Event-by-Event Monte Carlo Simulation of Radiation Transport in Vapor and Liquid Water

by

Georgios Ioannis Papamichael

B.A. (Mathematics) University of Cambridge, 1989
M.S.E. (Operational Research) Johns Hopkins University, 1991
Sc.M. (Applied Mathematics) Brown University, 1992

Thesis

Submitted in partial fulfillment of the requirements for
the Degree of Doctor of Philosophy
in the Division of Applied Mathematics at Brown University

May 2009

This dissertation by Georgios Ioannis Papamichael is accepted in its present form by the Division of Applied Mathematics as satisfying the dissertation requirement for the degree of Doctor of Philosophy

Date…… ……..……..……..

Dimitris Emfietzoglou, Director

Recommended to the Graduate Council

Date…… ……..……..……..

Martin R. Maxey, Reader

Date…… ……..……..……..

Lawrence Sirovich, Reader

Approved by the Graduate Council

Date…… ……..……..……..

Sheila Bonde, Dean of Graduate School

The Vita of Georgios Papamichael

Georgios Papamichael was born on May 24, 1968 in Athens, Greece. He graduated from Athens College in 1986. During his school years he showed special interest in mathematics and natural sciences. After succeeding in the GCE and CCE examinations he entered Trinity College of the University of Cambridge where he received a broad background in pure and applied mathematics. He received his BA degree with honors and was admitted to the Johns Hopkins University in a Master's degree program in Operational Research. He received his M.S.E. degree in 1991 and joined Brown University, where he received his Sc.M degree in 1992 in Applied Mathematics. In 1994 he returned to Greece and joined the army. After completing the military service he worked as a tutor for high school and undergraduate students. In 2000 he started a collaboration with the University of Ioannina as Research Associate, creating and developing the Monte-Carlo Radiation Transport Simulation code that carried out the numerical issues of the work presented here.

Scholarships & Assistantships

- Junior Scholar, University of Cambridge, 1990.
- Senior Scholar, University of Cambridge, 1991.
- Teaching Assistantship, Johns Hopkins University: Introductory Statistics for Business and Economics.
- Teaching Assistantship, Brown University: Introduction to Mathematical Methods, Introduction to Mathematica, Introduction to Asymptotics.
- Research Assistantship, Brown University: Low Dimensional Modeling for Transition and Turbulence in Channel Flow.

Publications in Peer-Review Journals

1. Emfietzoglou D., Papamichael G., Moscovitch M. An event-by-event computer simulation of interactions of energetic charged-particles and all their secondary electrons in water, *J. Phys. D: Appl. Phys*., **33**:932-944 (2000).
2. Emfietzoglou D., Papamichael G., Kostarelos K., Moscovitch M. A Monte-Carlo track structure code for electrons (~10 eV-10 KeV) and protons (~0.3-10 MeV) in water: partitioning of energy and collision events, *Phys. Med. Biol*., **45**:3171-3194 (2000).
3. Emfietzoglou D., Papamichael G., Moscovitch M. Monte-Carlo simulation of charged particle transport in bio-matter, *Phys. Medica*, **17**:113-114 (2001).
4. Emfietzoglou D., Papamichael G., Moscovitch M. Charged particle interactions in water: cross sections and simulations, *Radiat. Phys. Chem*., **61**:597-598 (2001) (www.sciencedirect.com).
5. Emfietzoglou D., Karava K., Papamichael G., Moscovitch M. Monte-Carlo simulation of the energy-loss of low-energy electrons in liquid water, *Phys. Med. Biol*., **48**:2355-2371 (2003).
6. Emfietzoglou D., Karava K., Papamichael G., Moscovitch M. Monte-Carlo calculations of radial dose and restricted-LET for protons in water *Radiat. Prot. Dosim*. **110**:871-879 (2004).

7. Emfietzoglou D., Papamichael G., Androulidakis I., Karava K., Kostarelos K., Pathak A., Moscovitch M. A Monte-Carlo study of sub-keV electron transport in water: the influence of the condensed-phase. *Nucl. Instrum. Meth*. **B228**:341-348 (2005) (www.sciencedirect.com).
8. Emfietzoglou D., Pathak A., Papamichael G., Kostarelos K., Dhamodaran S., Sathish N., Moscovitch M. A study on the electronic stopping of protons in soft biological matter. *Nucl. Instrum. Meth*. **B242**:55-60 (2006) (www.sciencedirect.com).
9. Emfietzoglou D., Paganetti H., Papamichael G., Pathak A. Monte-Carlo calculation of nanoscale dosimetric distributions of MeV proton tracks with secondary electron transport. *Nucl. Instrum. Meth*. **B245**:80-84 (2006) (www.sciencedirect.com).
10. Emfietzoglou D., Nikjoo H. Papamichael G., Pathak A. Proton beam profiling in soft biological matter by detailed Monte-Carlo simulation. *Nucl. Instrum. Meth*. **B249**:670-672 (2006) (www.sciencedirect.com).
11. Emfietzoglou D., Papamichael G., Karava K., Androulidakis I., Pathak A., Phillips G.W., Moscovitch M., Kostarelos K. A Monte-Carlo code for the detailed simulation of electron and light-ion tracks in condensed matter. *Radiat. Prot. Dosim*. **119**:491-496 (2006).
12. Emfietzoglou D., Papamichael G., Pathak A., Fotopoulos A., Nikjoo H. A Monte-Carlo study of energy deposition by heavy charged-particles in sub-cellular volumes. *Radiat. Prot. Dosim*. **126**:457-462 (2007)

Publications in Conferences

1. Emfietzoglou D., Papamichael G., Moscovitch M. Monte-Carlo Simulation of Charged Particle Transport in Biomatter, *1st International Workshop on Space Radiation Research and NASA'S 11th Annual Workshop on Space Radiation Health*, Aaron, Italy, p. 25 (2000)
2. Emfietzoglou D., Papamichael G., Moscovitch M. Charged Particle Interactions in Water: Cross Sections and Simulations, *8th International Symposium on Radiation Physics*, Prague, Czech Republic, p. 120 (2000)

Abstract of “Event-by-Event Monte Carlo Simulation of Radiation Transport in Vapor and Liquid Water”, by Georgios Ioannis Papamichael, Ph.D., Brown University, May 2009

A Monte-Carlo Simulation is presented for Radiation Transport in water. This process is of utmost importance, having applications in oncology and therapy of cancer, in protecting people and the environment, waste management, radiation chemistry and on some solid-state detectors. It’s also a phenomenon of interest in microelectronics on satellites in orbit that are subject to the solar radiation and in space-craft design for deep-space missions receiving background radiation. The interaction of charged particles with the medium is primarily due to their electromagnetic field. Three types of interaction events are considered: Elastic scattering, impact excitation and impact ionization. Secondary particles (electrons) can be generated by ionization. At each stage, along with the primary particle we explicitly follow all secondary electrons (and subsequent generations). Theoretical, semi-empirical and experimental formulae with suitable corrections have been used in each case to model the cross sections governing the quantum mechanical process of interactions, thus determining stochastically the energy and direction of outgoing particles following an event. Monte-Carlo sampling techniques have been applied to accurate probability distribution functions describing the primary particle track and all secondary particle-medium interaction. A simple account of the simulation code and a critical exposition of its underlying assumptions (often missing in the relevant literature) are also presented with reference to the model cross sections. Model predictions are in good agreement with existing computational data and experimental results. By relying heavily on a theoretical formulation, instead of merely fitting data, it is hoped that the model will be of value in a wider range of applications. Possible future directions that are the object of further research are pointed out.

Acknowledgments

My thesis is dedicated to my parents Giannis and Eleni, my sister Marianna for all their love and support, to my son George and to the memories of my uncle Jimmy.

I would like to thank my advisor Prof. Dimitris Emfietzoglou for providing financial support throughout the course of this research, his valuable input on the quantum physics and for providing the appropriate formulae for calculating the interaction cross-sections.

I would like to express my gratitude to Prof. Lawrence Sirovich who, with his long-term commitment to research, always provided me with wisdom and insight. His supervision during this collaboration was vital.

I thank Prof. Martin Maxey for his enthusiastic encouragement and guidance during the write-up stage of the dissertation.

Many thanks to the staff of the Division of Applied Mathematics, especially to Jean Radican for doing her share of the submission process.

I would like to thank Dr. Dingfelder and Dr. Uehara for providing data for comparison in the electron calculations. Also my thanks to Dr. H. Nikjoo for providing raw data from the code KURBUC and for his valuable comments on the manuscript of the paper presented in Chapter 2.

Contents

List of Tables

List of Figures

Chapter 1

Introduction

1.1 Cross-section and probability

Radiation Transport is the process of slowing down an ejected particle penetrating into a medium. We call this the *primary* particle. Thus, energy is transferred from the primary particle to the medium through a series of interactions or *events*, during which the particle interacts with the building elements of the medium, atoms or molecules.

The most fundamental assumption affecting the positioning of events is that the probability of interaction of a moving particle per unit length in the direction of motion per target is a constant independent of time and therefore distance in that direction. In probabilistic terms this property is referred to as *memorylessness*. The only memoryless distribution is the exponential and therefore the distance X until an event takes place follows the exponential distribution with some parameter σ.

In general, the notation

$$Z \sim PDF(parameters) \tag{1.1}$$

will be used to denote the probability density function of a random variable *Z*. In the case of distance to next interaction (DNI), *X* we have

$$X \sim EXP(\sigma) \tag{1.2}$$

or, equivalently,

$$\Pr(X \in (x, x+dx)) = \sigma \exp(-\sigma x)dx, \quad x > 0. \tag{1.3}$$

The constant σ is referred to as the *cross-section*. Different interactions act independently. More specifically, if an elastic scattering is to take place at distance $X_{elastic}$, an excitation at $X_{excitation}$ and an ionization at $X_{ionization}$ we have

$$\begin{aligned} X_{elastic} &\sim EXP(\sigma_{elastic}), \\ X_{excitation} &\sim EXP(\sigma_{excitation}), \\ X_{ionization} &\sim EXP(\sigma_{ionization}) \end{aligned} \tag{1.4}$$

and the distance to the next interaction experienced will be

$$X = \min(X_{elastic}, X_{excitation}, X_{ionization}) . \tag{1.5}$$

Under the assumption that $X_{elastic}$, $X_{excitation}$ and $X_{ionization}$ are independent random variables, it can be shown that

$$X \sim EXP(\sigma_{total}) , \tag{1.6}$$

with

$$\sigma_{total} = \sigma_{elastic} + \sigma_{excitation} + \sigma_{ionization} . \tag{1.7}$$

The type of interaction experienced will be elastic scattering if $X=X_{elastic}$, excitation if $X=X_{excitation}$, and ionization if $X=X_{ionization}$. One calculates the corresponding probabilities as

$$\begin{aligned} \Pr(elastic) &= \frac{\sigma_{elastic}}{\sigma_{total}}, \\ \Pr(excitation) &= \frac{\sigma_{excitation}}{\sigma_{total}}, \\ \Pr(ionization) &= \frac{\sigma_{ionization}}{\sigma_{total}}. \end{aligned} \tag{1.8}$$

It then follows that the number of events for a given distance *x, N(x)* is a Poisson process with parameter σ_{total} :

$$\Pr\left(N(x)=k\right) = \frac{(\sigma_{total}x)^k}{k!}\exp(-\sigma_{total}x),\ k=0,1,... \tag{1.9}$$

The formulae in equation (1.2) and (1.8) can be used for calculating the DNI and type of interaction for a single collision (see Chapter 7 for detailed calculation). In practical terms if one knows the cross sections one can describe the next interaction.

Although this is a good way of determining single collision data, in the radiation transport problem it is inaccurate, since the cross-sections depend on the energy of the relevant particles, which changes discontinuously between events. Therefore no analytic solution to the transport process is possible. This necessitates the use of Monte-Carlo Simulations.

1.2 Physics of particle-medium interactions

Suppose E is the energy transfer in an inelastic collision, $\frac{d\sigma}{dE}$ defines a spectrum or *pre-probability* density function for E. It is a non-negative, integrable function that may be normalized appropriately to form a probability density function. The independent argument of σ follows the corresponding probability distribution.

The cross-section determines all the physical quantities of interest: Defining the *moments* of σ as

$$\sigma^{(k)} = \int_{E_{\min}}^{E_{\max}} E^k \frac{d\sigma}{dE} dE \quad k = 0,1,2,\ldots, \tag{1.10}$$

the Inverse Mean Free Path (IMFP) is expressed as

$$\mu = n\sigma^{(0)} \tag{1.11}$$

and the Mean Free Path (average event-to-event distance) as

$$\lambda = \frac{1}{\mu}. \tag{1.12}$$

Here n is the density of targets in the medium. The average loss of energy of a charged particle per unit distance in the direction of motion (the stopping power) is

$$S = n\sigma^{(1)}, \tag{1.13}$$

the average energy transfer in the collision

$$\langle E \rangle = \frac{\sigma^{(1)}}{\sigma^{(0)}}, \tag{1.14}$$

and the Straggling Parameter – a measure for the spread of energy transfer

$$\Omega = \sqrt{n\sigma^{(2)}}\ . \tag{1.15}$$

When *elastic scattering* takes place the total kinetic energy of the particle-target system remains constant. Elastic scattering thus is responsible for energy transfer and deflection of the incoming particle. *Inelastic scattering* takes place when there is non-zero energy transfer from KE of particle to potential energy of the target. It is characterized as *excitation* or *ionization*. Excitation is an elevation in energy level of the target above the ground state. The lifetime of the target in an excited state is usually short: spontaneous emission of a quantum of energy (such as a photon) usually occurs shortly after the target is promoted to the excited state, returning the system to a state with lower energy (a less excited state or the ground state). Ionization is the process of converting an atom or molecule into an ion by removing a charged particle such as an electron. The free electron generated is called a *knock-on* electron. If the cross-sections are known one can calculate the energy and direction of the scattered particle and the knock-on electron after an ionization event. High energy knock-on electrons that quickly escape the volume of interest are also referred to as "δ-rays".

Since the minimum energy required for ionization depends on the particular atom or molecule as well as its state (gas, liquid, solid) there cannot be an explicit differentiation between ionizing and non-ionizing radiation. During an ionization

event the atom/molecule absorbs an amount of energy at least equal to the ionization cutoff (~10 eV) which is greater than the energy that binds a typical chemical bond (~5 eV). The greatest importance of ionizing radiation from a biologist's point of view is that it can break randomly chemical bonds in bio-matter. In the human and animal body there exist continuously free electrons whose KE is relatively small (typically<<1 eV). Thus they cannot produce ionizations and cannot alter the chemical bonds of cells. When the KE of the charged particles is large enough (>10 eV) (e.g. originating from nuclear reaction) their interaction with the atoms or molecules of the medium can create a knock-on electron by transferring part of their kinetic energy to the target. They can be characterized as ionizing radiation and are able to break chemical bonds in the medium. Knock-on electrons produced by ionization events may have themselves KE>10 eV and thus can create further ionizations. Those are referred to as *secondary* particles. Secondary electrons with KE from a few eV to some keV are the most important source of inelastic scattering in the medium.

Inelastic scattering is characterized as *coherent* or *incoherent* scattering. Coherent scattering takes place when the incoming particle is scattered simultaneously from many scattering centers (atoms or molecules). In coherent scattering the incoming radiation's wavelength is at least of the same order of magnitude as the inter-atomic/molecular distances in the medium. Therefore the relevant particles must be described quantum-mechanically by a wavefunction. The uncertainty principle prohibits the complete determination of the particle's

momentum and position simultaneously and therefore it is meaningless to talk about a particle trajectory. Coherent scattering gives rise to interference effects that lead to diffraction. It is unimportant in liquids and amorphous solids due to the randomness of atomic positions. Incoherent scattering takes place when the incoming particle is scattered by single scattering targets *one at a time*. This assumption is justified when the incoming radiation's wavelength is small compared to the inter-atomic/molecular distances. The relevant particles may be considered as classically-behaved between collisions and therefore have a well-defined trajectory. In this semi-classical approximation quantum mechanics is used only at the instant of interaction. In this vein, in the between-event intervals we have a stack of particles with definite position, momentum and energy.

1.3 Methodology of Monte-Carlo simulation

Despite the fact that all MC codes, by their nature, are computationally intensive, they allow for the study of the random nature of a particle's track and thus the statistical fluctuations of various stochastic quantities may be obtained. In principle, the sophistication of the technique is merely limited by the availability of the appropriate physical input, i.e. the interaction cross-sections. In that respect, the results obtained are, at best, as good as the input information incorporated in the code. Therefore, a sufficiently detailed presentation of the underlying physics must always accompany the documentation of such codes. Analytic and computationally

practical representations of the cross-sections for the considered interactions are prerequisites for following the discrete slowing down process and storing all of the details. Thus in each case the model cross-sections developed are presented in some detail.

Although several similar codes for the analysis of track structure have been developed (see [100] and references therein), they all differ in the exact treatment of the particular interactions; most importantly the secondary-electron spectrum. In the present study, the consistent theoretical framework of Bethe's theory has been employed, taking also into account well established experimental data.

The entire secondary electron energy spectrum has been modeled by a semi-empirical approximation combining the leading term of Bethe's asymptotic cross-section with an appropriate binary collision formula. The elastic scattering cross-section was modeled by a modified Rutherford formula that accounts for screening, while impact excitation was modeled by an empirical formula which exhibits the correct (Born–Bethe) asymptotic behavior. Binding effects for the most important molecular transitions are explicitly accounted for by partial inelastic cross-sections. By following the histories of all particles, the code scores the spatial coordinates of all elastic and inelastic collision events, as well as the partitioning of energy loss to the various inelastic channels.

A widely reported conclusion in studies investigating the effects of ionizing particles is that the response of the irradiated object (being a detector or a living cell) does not solely depend on the radiation dose, i.e. the average amount of

radiant energy absorbed in it but also on the energy spectrum and type of particles delivering it. The explanation usually put forward is that the presence of such a particle-dependent result is a consequence of the different structure (i.e. spatial distribution of collisions and energy deposition) of charged-particle tracks in irradiated matter [121, 64]. This has been the case in a variety of diverse circumstances, such as, in the study of radiolytic species in radiation chemistry [133], the health risk from radiation-induced biological damage [65] and the radiation response of some solid state detectors [61].

As an example consider the DNA in the core of a living cell in the form of a double helix. It consists of nucleotides bonded in pairs. Suppose we have an event that destroys one of the nucleotides. The DNA emerges in an environment chemically rich in free nucleotides, and soon a nucleotide of the appropriate type takes the place of the destroyed nucleotide and completes the chain, thus repairing the DNA. However if both nucleotides of a pair are destroyed, the information as to what type of nucleotides were there is permanently lost and the DNA breaks up into two. This can have devastating results for the cell's evolution. The best case scenario is that the cell might just die out. If the cell does not die, it may start to anomalously replicate forming a cancer tumor. We therefore need to calculate along with the total energy deposited in the medium, a measure of the dispersion of energy deposited. In particular the complete spatial distribution of energy deposition is desired.

The current tendency to progressively focus on very small volumes (e.g. at the micro- or even nano-metre scale) enhances the need for a stochastic treatment since, all other things being equal, the smaller the irradiated volume the larger the statistical fluctuations in it. Thus, a Monte-Carlo (MC) based event-by-event transport simulation is the preferred method for stochastic track structure calculations [109, 100]. The term event-by-event denotes a full three-dimensional representation of the interactions taking place during the particles' slowing down process, in terms of position, type, and energy transfer, according to appropriate single-collision cross-sections. Such an analysis should be contrasted with the common MC codes used for macroscopic applications (e.g. EGS, ETRAN) [120]. The term macroscopic implies that the spatial resolution acquired is large relative to the mean free path of the charged particles. These codes adopt the condensed-history approach [9] whereby the path is divided into a number of steps during which the effect of several interactions is handled together by appropriate multiple-scattering theories. Thus, such codes are generally inappropriate for a detailed analysis at the atomic/molecular level.

Chapter 2

Monte-Carlo simulation of the energy loss of low-energy electrons in liquid water

2.1 Introduction

Detailed Monte-Carlo (MC) codes simulating event-by-event the slowing-down of electrons in water have been a valuable tool in elucidating, in quantitative terms, radiation action at the molecular level [101]. In particular, such codes have been extensively used in the field of microdosimetry in understanding the biophysical basis of low-dose (or single-track) effects [46, 121]. Modeling the spectrum of possible DNA damage has been a key product of this line of research, revealing the prominent role of low-energy (sub-keV) electrons within the clustered-damage hypothesis [96, 47, 85, 141, 97].

Low-energy electron transport, however, poses serious challenges owing to the failure of classical cross-section models at this range [76]. This is basically the

reason why the general-purpose MC codes are, by and large, high energy approximations (>10–100 keV). The target electrons are treated as being free, with the effect of binding accounted only roughly [30]. Modeling energy losses of comparable magnitude to electronic binding energies necessitates that target-specific inelastic cross-sections are used, properly accounting for the electronic degrees of freedom of the system.

Low-energy electron transport simulation in water has been mostly performed within the so-called gas-phase approximation, i.e. cross-section models for the free-molecule have been linearly extrapolated to the unit density environment of the liquid [154, 109, 71, 135, 80, 143, 35] (see also [101] and [136] for a comparative discussion). The availability of experimental cross-section data for the elastic and inelastic scattering of electrons off vapor water has been the core justification behind this practice. It is generally recognized that, though incomplete, the available data are adequate to support empirical cross-section models of sufficient accuracy. In contrast, experimental data for the liquid are limited to either the optical limit or the Bethe-ridge [25]. Therefore, it is necessary to perform interpolations and/or extrapolations to cover the entire Bethe-surface of liquid water which, given the complexity of the underlying theory, are very much model-dependent [32]. Additionally, the use of such data is bound to the first Born approximation (FBA) and, therefore, modifications–of even larger uncertainty–are introduced into the models at lower energies to account for deficiencies of the FBA. Again, such considerations are often redundant for the vapor, since

experimental data down to a few tens of eV of electron impact are available; though of increasing uncertainty.

Differences in the optical absorption spectrum – which directly influence the soft-collision spectrum – between the vapor and liquid phases of water have been well documented [57]. In particular, the upward shift of the oscillator-strength due to condensation has been largely responsible for differences in track-structure characteristics calculated by vapor and liquid MC codes [133, 109]. Moreover, since the differences pertain to the biologically critical nanometer scale, important implications for the clustering properties at the DNA level may be anticipated [98, 153]. Several MC codes have been developed for simulating electron transport directly in condensed water [128, 113, 152, 119, 59, 15, 22] see also [63]. A detailed study for constructing electron inelastic cross-sections for liquid water at a form amenable for MC transport has been given [26] and subsequently used in the code PARTRAC for biophysical modeling [5, 45], whereas electron inelastic characteristics in a variety of tissue-equivalent materials including water have been calculated by Akkerman [1]. The work by Dingfelder and co-workers has been a sophisticated improvement of the extended-Drude model of Ritchie and co-workers used in the OrREC liquid water code [56, 117]. The calculations by Akkerman [1], on the other hand, follow a slightly different version of the extended-Drude model proposed by Ritchie *et al* [116]. Both models start from the construction of an optical-data model, which is then extended to the momentum space by an approximate dispersion scheme. This methodology has also been employed in the

liquid water code of Pimblott *et al* [113], as well as, in the general-purpose codes LEEPS [44] and PENELOPE [7] which are capable of handling low-energy electrons as well [124]. Along this line, we have recently provided an improved parameterization of the optical data of liquid water, which, additionally, is computationally more tractable than Dingfelder's (see [31]). Low-energy electron mean-free-paths and stopping-power values calculated by the model are in good agreement with the literature [38].

The present work extends our prior MC track-structure code for water vapor [35] to liquid water by incorporating a dielectric model for the liquid. The chapter is structured as follows. In the next section we present the basic cross-section input of our liquid code, emphasizing those aspects which mark a departure from our earlier MC code for the vapor. In particular, the dielectric model and its parameterization in terms of Bethe's asymptote are discussed in some detail. In the Results section we compare our dielectric cross-sections with other studies and provide energy-and interaction-point-kernel distributions for liquid water. The effect of various theoretical assumptions is examined.

2.2 The Monte-Carlo code

2.2.1 Inelastic dielectric model

For sufficiently energetic electrons, the first Born approximation (FBA), with the plane-wave assumption, provides an accurate description of the inelastic scattering process. For condensed targets, it is appropriate to treat the electron-matter interaction using the dielectric properties of the medium [82, 62, 115], and write the doubly-differential inelastic cross-section as follows:

$$\frac{d^2\Sigma}{dE\,dq} = \frac{1}{\pi\alpha_o Tq}\,\mathrm{Im}\left[\frac{-1}{\varepsilon(E,q)}\right] \tag{2.1}$$

where α_o is the Bohr radius, T the kinetic energy of the incident electron, ε the dielectric function of the target, Σ the macroscopic cross-section (in 1/length; called the inverse mean-free-path, IMFP), and E and q the energy- and momentum-transfer in the collision, respectively. Note that equation (2.1) refers to non-relativistic projectiles, which are of interest here. Corrections to equation (2.1) that account for deficiencies of the FBA at lower energies will be discussed in section (2.2.3). The Im[–1/ε(E,q)] term, called the energy-loss-function (ELF), is the important quantity in this context and it is inherently connected to the complex dielectric-response-function (DRF), ε (=ε_1+iε_2), by means of Im[–1/ε]=$\varepsilon_2/(\varepsilon_1^2+\varepsilon_2^2)$. It depends on both the atomic composition and, most importantly here, the phase-state of the material. It may formally be obtained by many-body quantum-

mechanical calculations, which, due to their computational complexity, are impractical to implement in a MC code. A widely used methodology for condensed targets, first employed by Ashley (see [4] and reference therein) and Ritchie *et al* (see [119] and reference therein), is to start by analytically representing the optical data (which pertain to the q≈0 limit) and then extend the so-obtained optical-data model to q>0 by an approximate, though physically realistic, dispersion scheme. The intention is twofold; first, to take advantage of any available experimental data, which, by default, include condensed phase effects (e.g. long-range polarization) and, second, to account in a self-consistent manner for the most important features of the Bethe-surface, thereby avoiding cumbersome theoretical calculations. The full ELF thus obtained, may then be used in equation (2.1) for calculating inelastic scattering probabilities (for both energy loss and angular deflection).

Details of the dielectric model along with a comparison with other studies may be found in [31] and [33]. Here, only a brief description will be provided. The dielectric model for liquid water is based on a Drude-parameterization of the optical data for the liquid of Heller *et al.* [58] and photo-ionization data for the vapor at higher energies. In this representation the optical dielectric-response-function takes the following form:

$$\varepsilon\left(E,0\right)=1+f_j\frac{E_p^2}{E_j^2-E^2-i\gamma_j E} \tag{2.2}$$

where E_p is the nominal plasma energy of the medium (≈21 eV for liquid water) and f_j, γ_j, E_j are the model oscillator strength, damping energy, and transition

energy for the inelastic channel j. It is then straightforward to obtain from equation (2.2) the imaginary part $\varepsilon_2 \equiv \mathrm{Im}(\varepsilon)$ which pertains to photon absorption. A linear superposition of such functions was then used in the de-convolution of the experimental $\varepsilon_2(E,0)$ spectrum to the various discrete and continuum transitions. In this procedure, the $\{f_j, \gamma_j, E_j\}$ were treated as empirical parameters determining, in effect, the height, width and position of the particular energy loss peak. Guided by the transition states of H_2O, five levels of excitations and four valence-shell ionizations were taken into account. In the decomposition of the optical spectrum, approximate binding energies of liquid water were used, whereas the excitation energies were adjusted by the fitting process. No collective excitations of the plasmon type were included, in accordance with the analysis of LaVerne and Mozumber [81]; this is also the position taken by Dingfelder and co-workers. In order to ensure that the model behaves reasonably well beyond the experimental range, which is limited to the low energy part of the spectrum, we used the relevant sum-rules and the I-value of the stopping-power theory as consistency checks:

$$\int_0^\infty E\varepsilon_2\left(E,0\right)dE = \frac{\pi}{2}E_p^2 \tag{2.3}$$

$$\int_0^\infty E\,\mathrm{Im}\left[\frac{-1}{\varepsilon\left(E,0\right)}\right]dE = \frac{\pi}{2}E_p^2 \tag{2.4}$$

$$\ln(I) = \int_0^\infty E\,\ln(E)\,\mathrm{Im}\left[\frac{-1}{\varepsilon\left(E,0\right)}\right]dE \Bigg/ \int_0^\infty E\,\mathrm{Im}\left[\frac{-1}{\varepsilon\left(E,0\right)}\right]dE \tag{2.5}$$

Eqs. (2.3) and (2.4) were satisfied to within 1-2% while an I-value at about 80 eV was obtained from equation (2.5). The extension to the momentum space followed the so-called extended-Drude formalism, where the q-dependence is inserted directly into the Drude parameters. It was first proposed by Ritchie and Howie [116] and later adopted in a somewhat different form in the OREC liquid code [119]. The latter version was adopted here where the impulse approximation is used for the continuum by making the substitution $E_{j,ioniz} \rightarrow E_{j,ioniz}(q) = E_{j,ioniz} + q^2/2m$, while an empirical GOS (generalized-oscillator-strength) for the free-molecule is adopted for the discrete, that is, $f_{j,exc} \rightarrow f_{j,exc}(q)$ from vapor experiments and, subsequently, $f_{j,ioniz} \rightarrow f_{j,ioniz}(q)$ from the f-sum-rule. The above scheme has also been used in the work of Dingfelder *et al* [26]. The ELF constructed by this procedure satisfies the two limits:

$$\lim_{q \to 0} \mathrm{Im}\left[\frac{-1}{\varepsilon(E,q)}\right] = \mathrm{Im}\left[\frac{-1}{\varepsilon(E,0)}\right]_{ODM} \tag{2.6}$$

$$\lim_{q \to \infty} \mathrm{Im}\left[\frac{-1}{\varepsilon(E,q)}\right] \approx \delta\left(E - Q\right) \tag{2.7}$$

where $Q = q^2/2m$ and ODM stands for the optical-data model.

2.2.2 Parameterization of the dielectric model

The dielectric model presented above provides a self-consistent procedure for calculating inelastic cross-sections for both the energy loss and the angular

deflection (the momentum transfer is directly related to the scattering angle by kinematics). Direct use of the doubly-differential cross-section, equation (2.1), however, is cumbersome, due to the q-dependence, necessitating a tabular form for use in an MC code. Therefore, it would be advantageous to develop an analytic energy-loss cross-section formula which will be able to reproduce the dielectric results but without the momentum-transfer (i.e. scattering angle) explicitly entering in the calculations. In view of the minor importance of inelastic collisions compared to the elastic ones in the angular deflection of low energy electrons, the de-coupling of energy and momentum appears, to a first-approximation, justified.

For inelastic collisions leading to secondary electron production (i.e. ionization) we employed a well-established methodology, first suggested by Miller and co-workers [87, 88, 86] and subsequently incorporated in the PITS code [143], which takes advantage of the asymptotic trends of Bethe's formula. For discrete inelastic events (i.e. excitations) we also use the Bethe asymptote with the addition of a modifying function, as proposed in [50]. The above methodology has also been used in our vapor code and, therefore, it provides a unified approach for both phases of water. It was found, however, that its application to the liquid phase is restricted to incident electrons above about 40-50 eV, due to the complete breakdown of Born-Bethe theory at even lower energies. The basic formula for ionization differential in secondary electron energy W reads as follows:

$$\frac{d\Sigma}{dW} = \frac{d\Sigma_{BOT}}{dW} + F(W)\frac{d\Sigma_{SCL}}{dW}, \tag{2.8}$$

where BOT stands for Bethe's optical term and SCL for semi-classical theory. For the latter, the binary-encounter-approximation (BEA) has been used [67]. In contrast to the vapor case, we used the non-corrected BEA form since the particular Born-corrections we have used here (see section (2.2.3) below) refer to both terms of equation (2.8). The BOT term, on the other hand, depends on the optical-oscillator-strength (OOS) of the target and may be written as:

$$\frac{d\Sigma_{BOT}^{(j)}}{dW} = \frac{4\pi\alpha_o^2 N}{T}\frac{R^2}{\left(W+B_j\right)}\frac{df^{(j)}(W,0)}{EdW}\ln\left(T/R\right), \tag{2.9}$$

where N is the molecular density and $df^{(j)}(W,q=0)/dW$ the OOS distribution for the j-th ionization shell. Phase effects may now be directly included in equation (2.9) by expressing the OOS in terms of the optical-ELF by means of:

$$\frac{R^2}{E}\frac{df(E,q=0)}{dE} = \frac{1}{8n\pi^2\alpha_o^3}\mathrm{Im}\left[\frac{-1}{\varepsilon\left(E,q=0\right)}\right] \tag{2.10}$$

where n is the density of electrons in liquid water. The optical-ELF in equation (2.10) is obtained by our optical-data model discussed earlier. As it has been analyzed in some detail elsewhere [36], equation (2.8) provides a good working model for the entire secondary electron energy spectrum and is particularly suitable for MC codes. The function F(W), essentially, moderates the contribution of collisions with non-zero momentum transfer, while not explicitly depending on the latter. Most importantly, it may be assumed to be independent of the projectile's energy since, to a good approximation, may be associated with the second-term of Bethe's asymptotic expansion (Emfietzoglou *et al* [36]).

The overwhelming contribution to inelastic losses at the energy range of interest here comes from the valence-shell electrons. For both the vapor and liquid phases, therefore, it was found sufficient to employ equation (2.8) for the four outer shells of water, while using a BEA-with-exchange (BEAX) formula, as provided by ICRU [67], for K-shell ionization. The justification for treating separately valence- and core-shell transitions has been discussed [1]. A comparison of our inelastic model with the model of these authors, which use a somewhat different dispersion scheme for the valence losses and Kim's binary model for K-shell ionization, has shown very good agreement in terms of electron inelastic mean-free-paths and stopping-powers for the energy range considered in the present study [38].

For the vapor phase, equation (2.8) was directly fitted to experimental data on $d\Sigma_{exp}/dW$ (after subtracting the calculated K-shell contribution) so as to determine $F_{vapor}(W)$. For the liquid, since such experimental data are not available, we use $d\Sigma_{diel}/dW$ data calculated by the dielectric model presented in section (2.2.1) to determine, by means of equation (2.8), the $F_{liquid}(W)$ (see Appendix A, (section 2.5.1)). By this procedure we were able to reproduce the dielectric differential cross-section data to within ±10% over the entire W-range down to 100 eV incident electron energies, and to within ±20% from 50–100 eV. Below 50 eV incident energies, the secondary spectra could not be accurately reproduced by equation (2.8). Similarly to the vapor phase, it was found necessary to subsequently use the total ionization cross-section Σ_{diel} for normalization. By means of the normalization function, $N_{diel}(T)$, the dielectric total ionization cross-sections were reproduced to

within ±1% over the entire range of incident energies (see Appendix B (section 2.5.2)).

For excitations which, by and large, result from low momentum-transfers we use Bethe's first-order term, but treat the OOS and the "momentum cut-off" [68] as adjustable parameters. The analytic representation of the excitation dielectric data was substantially improved by the introduction of an "adjusting" function, which operates at low-energies and is similar to that first proposed by Green and Stolarski [50]. After introducing the ELF (see equation (2.10)), the excitation cross-section in macroscopic units for transition to state j may be written as follows:

$$\Sigma_j = \frac{A_j}{2\pi\alpha_o}\left(B_j/T\right)\ln\left(C_j\frac{T}{R}\right)\left[1-\left(B_j/T\right)\right]^{P_j} \qquad (2.11)$$

where B_j are the excitation energies and A_j, C_j and P_j are the adjustable parameters the values of which were determined by fitting the relevant dielectric cross-section data for each discrete transition (see Appendix C (section 2.5.3)). Equation (2.11) was able to reproduce the dielectric data to better than 1%.

2.2.3 Low energy corrections

At energies where the projectile may no more be considered as fast compared to the orbital electrons with which it interacts, the FBA is known to gradually overestimate the cross-section and, eventually, fail. Thus, for incident

electrons and at energies below about 500 eV, the FBA results need to be corrected for higher-order perturbation terms which account for the distortion of the projectile's wave-function as it is scattered by the Coulomb field of the target, as well as, for the exchange effect between the incident and target electrons due to Pauli's principle. The importance of such corrections becomes apparent if one recognizes that they operate at the energy range where the inelastic cross-section maximum lies (~100 eV for electrons).

In our vapor code, Born-corrections were established empirically by adjusting our total cross-section values to the experimental data, which are available down to the eV range. Unfortunately, no such data are available for liquid. The complexity of the underlying theory has led to largely heuristic schemes for implementing the above effects to condensed-matter MC codes. In the present work, following Tung and co-workers (see [131] and reference therein), perturbation corrections were accounted for by the inclusion of a second-order term, whereas a Mott-type exchange modification was applied to the ionization part of the inelastic cross-section. The second-order correction formula for inelastic losses (i.e. both ionizations and excitations) reads as follows:

$$\frac{d\Sigma_{(2nd)}}{dE} = -\frac{2}{\pi\alpha_o T}\,\mathrm{Im}\left[\frac{-1}{\varepsilon(E,0)}\right] L(E) \qquad (2.12)$$

where $L(E) = (\hbar/\alpha_o)\,[E / [2T(2Tm)^{1/2}]] \times I(\xi)$ with $\xi = \frac{1}{2}\,(E/T)^{1/2}$ [72]; the analytic form of $I(\xi)$ is provided by Ashley [4]. Equation (2.8), however, is inadequate at

the lowest energy range (below about 100 eV) where the function L(E) becomes negative for certain values of E. A simple Coulomb-field correction was therefore adopted for T<100 eV as suggested by Vriens [138], i.e. the cross-section at an incident energy T is calculated instead at $T+B_j+U_j$, where B_j and U_j are the binding and kinetic energy, respectively, of an electron at the j-th orbital. This simple approximation has been found adequate by many investigators [125, 84, 60].

The exchange correction terms were obtained by analogy to the Mott formula:

$$\frac{d\Sigma_{Ex}^{(j)}(W,T)}{dW} = \frac{d\Sigma^{(j)}(T-W-B_j,T)}{dW} - \left[\frac{d\Sigma^{(j)}(W,T)}{dW} \times \frac{d\Sigma^{(j)}(T-W-B_j,T)}{dW}\right]^{1/2} \tag{2.13}$$

where each term in equation (2.13) should be understood as applied to the sum of the first- and second-order term of the differential ionization cross-section. Note that the BEAX formula [67] used for the K-shell ionization does contain an exchange and Coulomb-field correction as discussed by Vriens [138].

2.2.4 Angular deflections

Due to the lack of available data on the deflection of electrons after elastic or inelastic scattering off liquid water, and in view of the general difficulties associated with tackling the problem theoretically, the methodology used in our vapor code have also been adopted for the liquid. To summarize, the screened-

Rutherford formula has been used for elastic scattering above 200 eV, whereas at lower energies the fitting formulae of Brenner and Zaider [17] were used. The angular distributions of the scattered and secondary electrons after ionization were obtained based on the kinematics of binary collisions and the data of Opal *et al* [107] as described by Grosswendt and Waibel [51]. It is anticipated that the above methodology, which appears adequate for the vapor, would predict angular deflections not too far off from what really happens in the liquid. To our knowledge, the extension of elastic models for the free-molecule to the liquid phase is presently the method of choice also adopted in other liquid water codes [153, 59, 22].

2.3 Results

Figure (2.1a) depicts differential-IMFP (DIMFP) distributions as a function of the energy-transfer for 1 keV electrons in liquid water. The dielectric results have been obtained by means of equation (2.1) using our optical-data model and the extended-Drude dispersion scheme as discussed in section (2.2.1). The Bethe results represent calculations using only the optical term of Bethe's asymptote (see Eqs. (2.9)and (2.10)). Results by Dingfelder *et al* [26], which also pertain to the liquid, are also presented for comparison. A further comparison with the latter study is shown in Figure (2.1b), where the discrete and continuous component of the DIMFP distribution for 1 keV electrons is shown. The dielectric approach used

by Dingfelder and co-workers is based on a somewhat different optical model (developed by the same set of data, though) while employing the same dispersion scheme. As it will become apparent below, for this electron energy the results are practically indifferent to the application of Born-corrections.

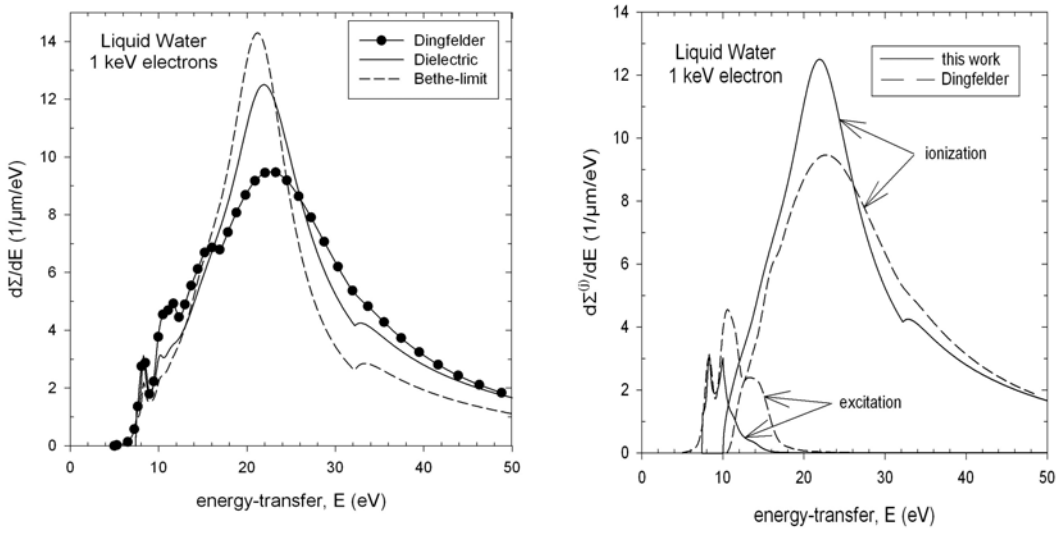

(a) (b)

Figure 2.1. Differential inelastic inverse mean-free-path versus energy transfer for 1 keV electron in liquid water: (a) Comparison of calculations using the dielectric model and Bethe's optical term. Results by Dingfelder *et al* [26] are also included. (b) The partitioning between excitation and ionization predicted by the present dielectric model and by Dingfelder *et al* [26].

Figures (2.2a) and (2.2b) reveal the effect of Born-corrections on the DIMFP distributions for the energy range 0.1-1 keV. In particular, in Figure (2.2a), first-order results for various incident energies obtained by equation (2.1) are compared to calculations incorporating both the second-order correction equation

(2.12) and the exchange correction equation (2.13). In Figure (2.2b) the effect of each type of correction is shown for the case of 100 eV incident electron. For comparison we have also performed calculations using Paretzke's low-energy correction, which has been established empirically from vapor data. Paretzke's correction has been used in the calculations of Dingfelder *et al* [26] as a second-order perturbation correction.

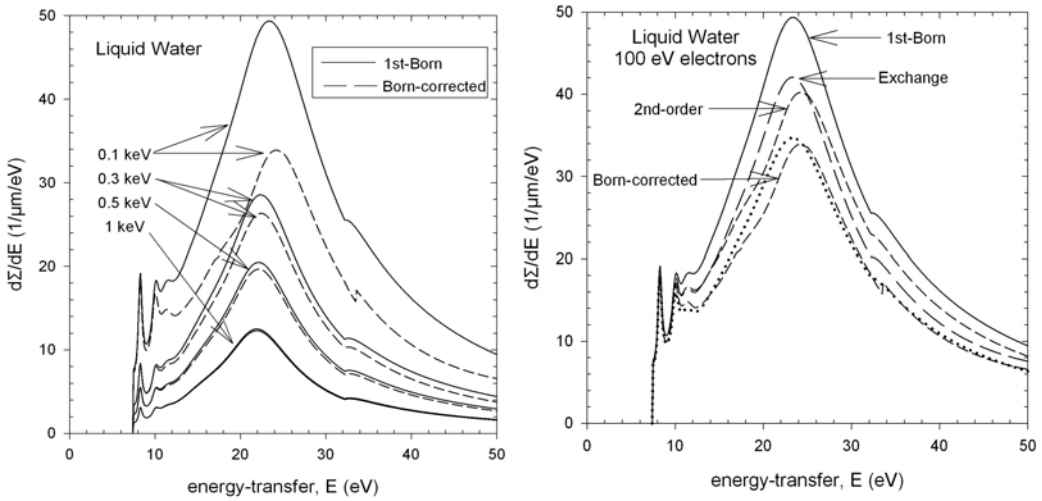

(a) (b)

Figure 2.2. Differential inelastic inverse mean-free-path versus energy transfer for various electron energies in liquid water using the first-order Born dielectric model supplemented by the various corrections: (a) Calculations with and without Born-corrections; (b) The effect of the second-order and exchange correction to the first-order Born model is explicitly shown for 100 eV electrons. The vapor based correction (see Dingfelder *et al* [26]) is also included for comparison (dotted-curve).

In Figure (2.3a) inelastic IMFPs calculated to first-order (Born), second-order with exchange (Born-corrected), and by the optical (Bethe) approximation, are compared to the predictions of Dingfelder *et al* [26], as well as, with the total

inelastic cross-sections for the vapor calculated by Uehara *et al* [136]. These results have been further analyzed in Figure (2.3b) in terms of the ionization efficiency, that is, the probability that an inelastic collision will result in an ionization event as opposed to excitation. In Figure (2.3c), the effect of the second-order and exchange corrections to the first-order Born IMFP results is depicted.

Figures (2.4a) to (2.4d) present energy point-kernel distributions for 0.2 keV, 0.5 keV, 1 keV, and 5 keV electron energies. For each distribution, 1000 starting electrons and all their secondaries have been followed down to 50 eV, and the energy deposited in spherical shells at 1 nm intervals from the track origin is scored and normalized to the total energy of the tracks. Simulations have been performed using both the first-order (Born) model and the Born-corrected model for determining electron differential and total inelastic probabilities (applied to both the primary and secondary electrons). To gain some insight into the influence of the various corrections on the track-structure, simulation results with each correction separately are also presented, i.e. either the second-order or the exchange correction added to the first-order Born model. The effect of the dispersion is also examined by running simulations using the optical (Bethe) approximation. In the case of 1 keV electron energy results from the vapor code KURBUC are also shown [136].

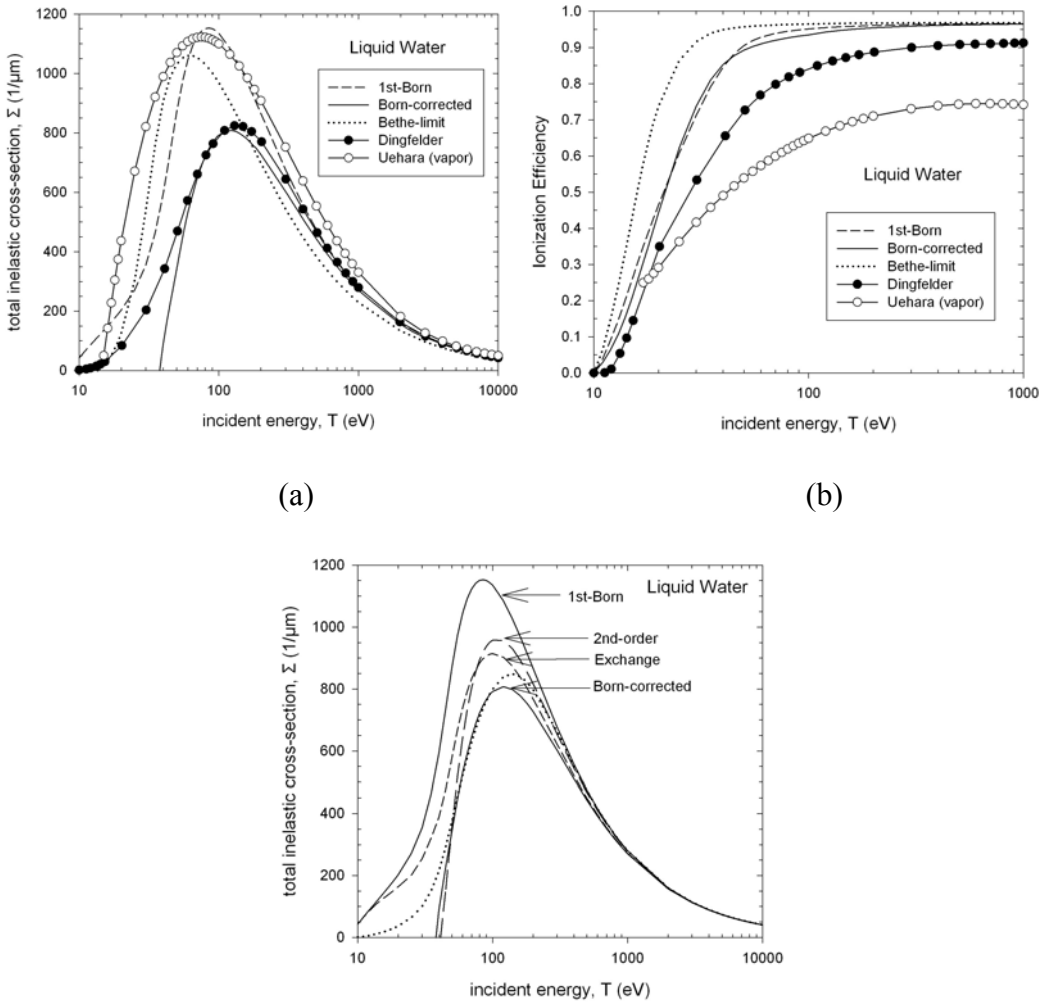

Figure 2.3. (a) Comparison of calculations of total inelastic inverse mean-free-path versus incident electron energy in liquid water using the dielectric model (with and without Born-corrections) and Bethe's optical term. Results by Dingfelder *et al* [26] for the liquid and by Uehara *et* al [136] for vapor are also included; (b) the ionization efficiency predicted by the models used in (a); (c) The effect of the second-order and exchange correction to the first-order Born model is explicitly shown. The vapor based correction (see Dingfelder *et al* [26]) is also included for comparison (dotted-curve).

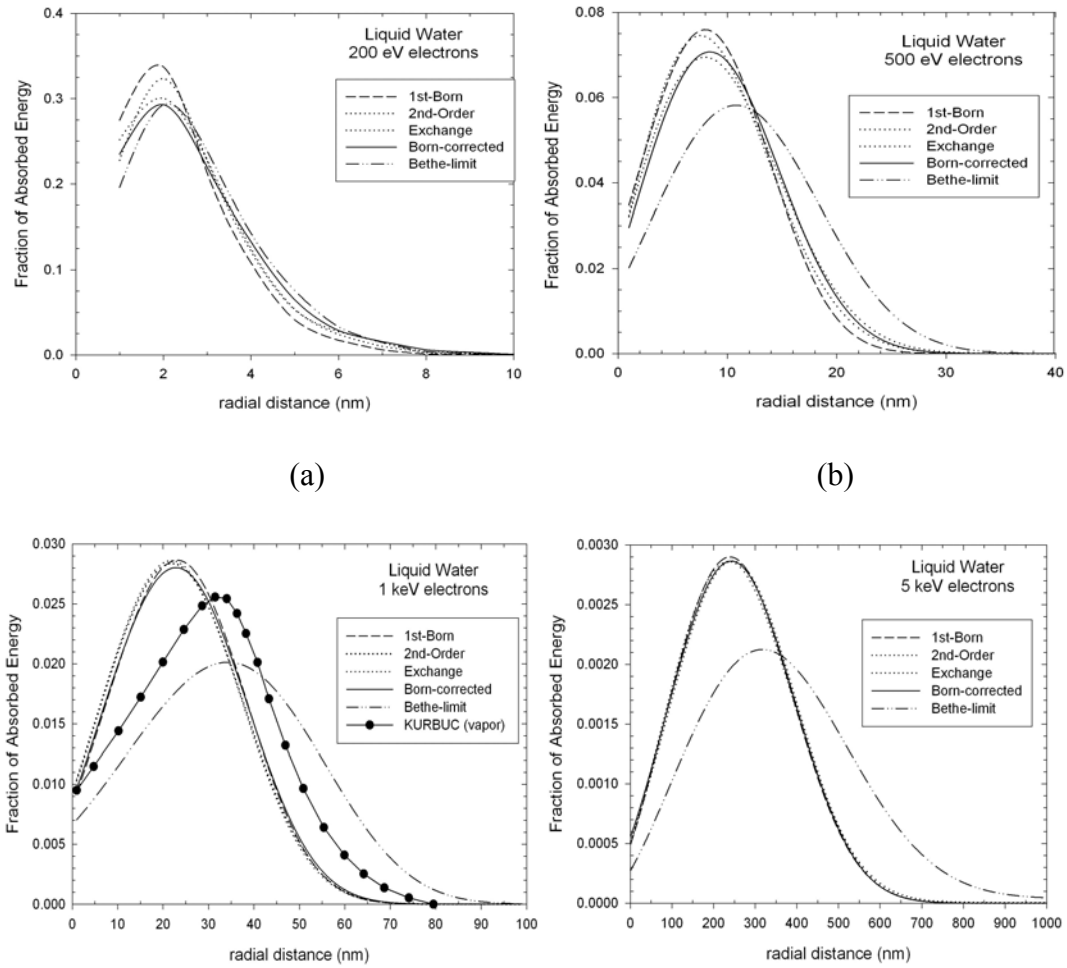

Figure 2.4. Comparison of energy point-kernel distributions for various electron energies calculated by the present dielectric model (with and without Born-corrections) and Bethe's optical term. The effect of the second-order and exchange corrections to the first-order Born model is explicitly shown. For 1 keV electrons results from the vapor code KURBUC are also included (Uehara et al [135]).

In Figures (2.5a) to (2.5d) (inelastic) interaction point-kernel distributions for the same electron energies and inelastic models as in Fig (2.4) are presented.

These radial distributions are expressed as complement cumulative percentage of interactions (CCPI) distributions normalized to the total number of interactions.

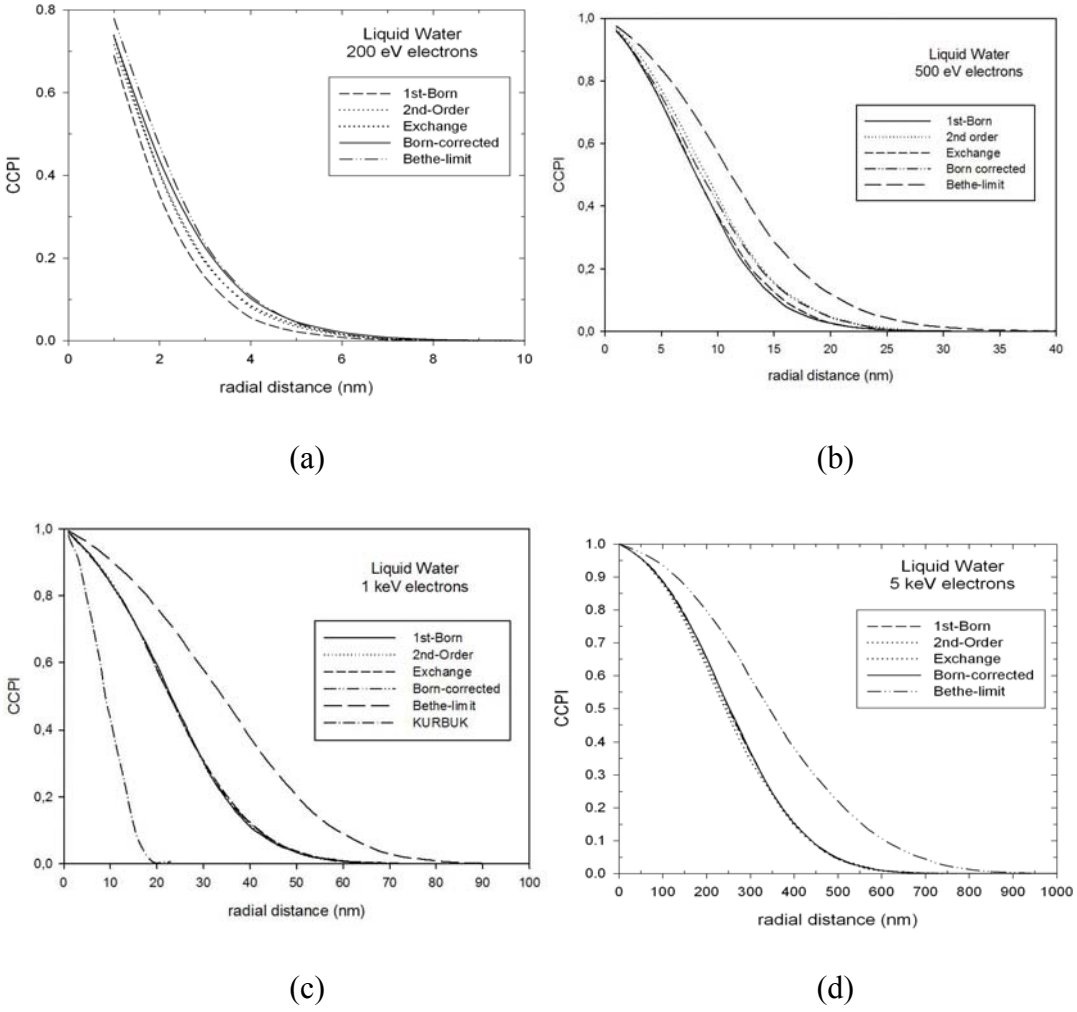

Figure 2.5. Comparison of interaction point-kernel distributions presented as complement-cumulative-probability of interactions (CCPI) for various electron energies calculated by the present dielectric model (with and without Born-corrections) and Bethe's optical term. The effect of the second-order and exchange corrections to the first-order Born model is explicitly shown. For 1 keV electrons results from the vapor code KURBUC are also included [135].

2.4 Discussion

The underlying physics input, in terms of cross-section models, of our Monte-Carlo code for event-by-event electron transport in liquid water has been presented in some detail. In particular, those aspects that mark a departure from our earlier developed MC code for vapor water have been emphasized. Simulation results from slowing-down electron tracks have been presented in terms of energy- and interaction-point-kernel distributions for low energy electrons in liquid water. In view of the wide use of the first Born approximation and the dielectric approach in modeling the inelastic interactions of low-energy electrons in condensed matter, we have undertaken calculations to shed some light on the effect of the dispersion and Born-corrections upon both the single-collision and the slowing-down distributions. Such a comparison, obviously, doesn't provide any justification for their use, but, nevertheless, may well be used for assessing their expected impact on track-structure calculations.

The transport scheme adopted in the present as well as in our vapor code remains bound to the trajectory picture, that is, the projectiles bear straight-line classical trajectories in between successive scattering events against individual molecules, which are further assumed to be randomly distributed. Thus, following the standard practice, coherent scattering events, which are possible at very low energies, are not accounted for. This appears to be well justified in the present code, where a cut-off at 50 eV is adopted; this was surely not the case, however, in

our vapor code with a 7.4 eV cut-off. Nevertheless, the adoption of the present cut-off was not made on the above grounds (since there is a general and tacit practice to neglect coherent effects in this type of studies) but from the fact that the theoretical formalism adopted failed at lower energies. It is expected that in the present form the code may be suitable for various energy loss track-structure calculations; it would most likely, though, be inadequate for modeling the subsequent chemical stage of radiation action. To a first approximation, one may overcome this problem by adopting the vapor code cross-sections at lower energies. A more self-consistent approach, of course, would be to use calculated dielectric data (for the liquid) implemented in tabular form. Alternatively, along the lines of the present treatment, one may still use some form of the Bethe asymptote by adding a low-energy "adjusting" function similar to the one used for the excitations. The main challenge would be to find an appropriate function for both the integral and differential distributions.

The results presented on the inelastic cross-section distributions reveal that the effects of dispersion and Born-correction are particularly noticeable at low energies in the single-collision regime. For example, the neglect of dispersion results in about 15% overestimation of the peak of the differential distribution at 1 keV electron impact (see Figure (2.1a)), whereas the reduction brought about by the Born-corrections becomes noticeable below about 500 eV, gradually reaching 45 % at 100 eV (Figure (2.2a)). The second-order and exchange corrections appear to contribute almost equally to the above reduction (Figure (2.2b)). Interestingly, the

second-order correction established empirically from vapor data and employed in the liquid calculations by Dingfelder *et al* [26], is almost twice as large as the second-order correction used here, which has been based on optical data for the liquid (Figure (2.2b)). Finally, from Figure (2.1a) considerable differences are observed with Dingfelder's and co-workers' results, despite the fact that for both models the global characteristics (sum-rules, I-value) are consistent with expected values. As discussed elsewhere [32], the differences are the result of the different parameterization used for representing the optical absorption spectrum. Judging from our own efforts, it appears that the use of a strong excitation component in Dingfelder's model prohibits the accurate representation of the prominent plasmon-like peak at about 21 eV as it may be seen from Figure (2.2) in [32]. (Note that the same arguments hold for the earlier work of Ritchie *et al* [119]). It should be highlighted though that given the limited available data for the liquid phase, the relative strength of the various transitions is largely model-dependent. As discussed in section (2.2.1), the parameterization of the optical spectrum performed is based on only a small number of physical constrains which, for the most part, are inferred from the vapor. A detailed discussion of this aspect with emphasis on the plasmon-like peak may be found in [78].

With respect to the integrated distribution, the effect of dispersion is noticeable at almost the entire energy range examined; calculations with the optical-approximation lead to an overestimation at the very low range and an underestimation at higher energies (Figure (2.3a)). The effect of Born-corrections, on the other hand, is only noticeable below 500 eV, as expected from Figure (2.2a), leading to an overestimation of about 40 % at the region of the peak (~100 eV). Note also that, due to the gradual failure of the second-order term at very low energies (<100 eV), the Born-corrected model depicted is increasingly inaccurate at this energy range. As discussed in section (2.2.3), a Coulomb-field correction has been introduced at the 50-100 eV range. A fundamental problem in having the present methodology extended below 50 eV is the analytic representation of the continuum by the application of equation (2.8), which has its roots in Bethe's theory. As explained in section (2.2.2), we were unable to accurately reproduce the secondary electron spectrum by means of equation (2.8) below about 50 eV incident energies.

From Figure (2.3b) it may be concluded that the effect of Born-corrections is practically negligible as far as the ionization efficiency is concerned. This is not the case, however, for the dispersion which appears to have a marked influence on the ionization efficiency below 100 eV. This is due to the fact that the relative strength of ionizations over excitations is essentially determined by their overall contribution in the Bethe-surface, which, in turn, depends also on the dispersion scheme used. As expected, the different parameterization used by Dingfelder and

co-workers which partitions more oscillator strength to excitations than our optical model (see also Figure (2.1b)) also leads to noticeable different predictions of ionization efficiency (despite the use of the same dispersion scheme in both studies).

Differences are also observed with the data of Uehara *et al* [136] which are based on vapor experiments (see Figs. (2.3a) and (2.3b)). The increasingly larger inelastic probabilities of the vapor over the liquid at low energies, especially below 100 eV, are the result of their different oscillator-strength at the important range from threshold to about 30 eV, that is, at the domain of the valence-losses which are mostly influence by the state of condensation. The prominent discrete peaks, characteristic of the vapor, are largely responsible for its higher oscillator-strength at this range. On the other hand, the enhanced ionization efficiency observed in the liquid is the result of the upward shift of the oscillator strength upon condensation, which, in turn, leads to a "harder" single-collision spectrum, thus, favoring ionization over excitation events (see [133] for an extended discussion).

Finally, similar to the case of the differential distributions, the second-order and exchange corrections appear to contribute equally to the integrated distribution as well, whereas Dingfelder's (vapor-based) correction leads to a reduction which is roughly twice as large as the (liquid-based) second-order correction used here (Figure (2.3c)).

Although an investigation of the effects of the various parameters on the single-collision distributions is by itself of direct relevance to the physics of

electron interaction with water, track-structure calculations are necessary to assess their impact on modeling the physical and subsequent stages of radiation action. A very basic track-structure characteristic for electrons in that respect is the point-kernel distribution which depicts the distribution of energy deposition (or interactions) around the point of origin of an electron beam in an isotropic and homogeneous medium. From Figures (2.4a) to (2.4d), and in accordance with the observations made above for the single-collision regime, the effect of Born-corrections appears to be of some importance below about 500 eV, whereas the effect of dispersion is noticeable at all energies. In particular, the point-kernel distributions calculated by the first-order cross-sections which overestimate the total inelastic probabilities at low energies and, thus, predict smaller inelastic mean-free-paths, result in somewhat higher energy deposition at shorter distances (i.e. closer to the track origin). For example, the effect based on the peak values is ~10% at 500 eV and 15% at 200 eV. In contrast, neglecting the dispersion by using Bethe's optical term, which predicts larger mean-free-paths (above ~100-200 eV), results in energy deposition at further distances for all energies studied. Comparison with results for electron tracks in vapor water calculated by the code KURBUC are depicted in Figure (2.4b) for 1 keV electrons. Despite the higher total inelastic probabilities for vapor (see Figure (2.3a)), and the concomitant smaller mean-free-paths, electrons deposit their energy at larger (density corrected) distances in the vapor case. This is due to the much smaller ionization efficiency of the vapor over the liquid (see Figure (2.3b)), which, on average, results in a smaller

energy loss per inelastic collision. Therefore, given the harder single-collision spectrum of the liquid, the energy distribution in the vapor predicted by KURBUC is extended to somewhat larger distances while a larger fraction of the absorbed energy is closer to the origin in the liquid. A similar conclusion was drawn in [24] for the case of 10 keV electron tracks.

Interaction point-kernel distributions, depicted as complement-cumulative-percentage of interactions (CCPI), reveal similar trends with the energy distributions discussed above. In particular, for the reasons stated earlier, it may be seen that the inclusion of Born-corrections tend to shift the point-kernel distribution of low energy electrons to larger distances by a few nm, whereas accounting for dispersion may result in a shift (to the opposite direction) of the order of 100 nm for the highest energy studied (5 keV). For the 1 keV case, the influence of phase appears to result in the shift of the distribution to higher distances by several nm. It should be pointed out that the possible existence of collective effects in the liquid phase may have a noticeable effect upon the track-structure calculations presented here, since it will affect both the yield of the various inelastic channels, as well as, the localization of the energy loss event.

2.5 Appendix

2.5.1 Appendix A.

The function $F_{liquid}(W)$ of equation (2.8) for liquid water, as determined from the calculated dielectric values $d\Sigma_{diel}/dW$ (see sections (2.1) and (2.2)), has the following polynomial form:

$$F_{liquid}(W) = \sum_{i=0}^{k} a_i \, W^i \tag{2.14}$$

where the order (k) and the fitting parameters (α_i) are given below:

	$1 \le W \le 25$	$25 < W \le 550$	$550 < W \le 4950$
k	8	4	2
α_0	0.035907	0.266516	0.851376
α_1	–0.057477	0.00487735	9.37477×10^{-5}
α_2	0.0318939	-1.8337×10^{-5}	-1.0811×10^{-8}
α_3	–0.010932	3.30427×10^{-8}	
α_4	0.00173459	-2.18872×10^{-11}	
α_5	–0.0001369		
α_6	5.70581×10^{-6}		
α_7	-1.2093×10^{-7}		
α_8	1.02986×10^{-9}		

Table 1. Coefficients of the power series expansion of the low-energy semi-classical correction term Fliquid(W) for ionization (equation(2.8)).

For $W > 4950$ one can safely assume that $F_{liquid}(W) = 1$.

2.5.2 Appendix B.

The normalization function $N_{liquid}(T)$, as determined by adjusting the integrated form of equation (2.4) to the calculated inelastic dielectric values $\Sigma_{diel}(T)$ for ionization (see sections (2.2) and (2.3)), has the following form:

$$N_{liquid}(T) = \left(1 - \frac{38.7266}{T}\right)^{0.1266} \tag{2.15}$$

2.5.3 Appendix C.

The parameters of equation (2.11), as determined by fitting equation (2.7) to the calculated inelastic dielectric values $\Sigma_{diel}(T)$ for each excitation level (see sections (2.2.2) and (2.2.3)), take the following values:

Excitation Transition, j	A_j	C_j	P_j	B_j (eV)*
1 (A^1B_1)	0.0205	4.9801	0.4757	8.22
2 (B^1A_1)	0.0209	3.3850	0.3483	10.00
3 (Ryd A+B)	0.0130	2.8095	0.4443	11.24
4 (Ryd C+D)	0.0026	1.9242	0.3429	12.61
5 (diffuse bands)	0.0025	3.4624	0.4379	13.77

Table 2. Fitting parameters for calculating the excitation cross-section (equation (2.11)) per excitation level.

*The transition energies B_j are given by the dielectric model. In the fitting procedure the B_j values are not allowed to vary.

Chapter 3

A Monte-Carlo study of sub-keV electron transport in water: The influence of the condensed-phase

3.1 Introduction

Electrons with kinetic energies in the sub-keV range, named here low-energy electrons (LEEs), play an important role in the mechanism of radiation action in matter by almost any sufficiently energetic particle beam [109]. The reason being that LEEs are abundantly produced during the slowing-down process and the dissipation of their energy is confined within sub-micron volumes. This spatial scale is often associated with important functional units in both biological systems and electronic devices. For example, cancer induction and cell-kill by radiation is supposed to be triggered by molecular events in the cell nucleus (few μm) associated with clustered damage in the DNA double-helix (few nm) and/or chromatin-size targets (10-100 nm) [97]. Due to the close proximity (nm-

separation) of successive ionization events in LEE tracks, their characteristic spatial pattern of interactions and energy deposition is by far more efficient compared to higher energy electrons in inducing clustered damage [96].

The study of LEEs, however, poses serious challenges due to the gradual failure of classical (binary) interaction models in the sub-keV range. The details of the electronic structure now become critical, giving rise to many-body effects in the scattering process. With respect to biological matter and the modeling of cellular radiation action, water has been traditionally the material of choice, being a realistic approximation of the cellular medium. The degree in which, however, condensed-phase effects (i.e. vapor vs. liquid phase at the same density) are important to modeling LEE tracks in water has been debated since the mid-70s; for a review see [63]. At the core of this debate lies the availability of well-established experimental cross-section data for the vapor phase, in sharp contrast to the limited information on the scattering properties of the liquid phase. Thus, vapor-based Monte-Carlo (MC) codes are generally considered more reliable than liquid-based MC codes, although the latter are supposed to be a more realistic approximation of the liquid-like cellular environment. However, the use of vapor data extrapolated linearly to unit density (i.e. the so-called gas-phase approximation of liquid water) neglects any non-linear density effects in the scattering process. The latter are known to be gradually more pronounced at low energies and, therefore, might be particularly important in modeling LEE tracks [133, 111, 99].

In the present study, we explore the influence of condensed phase (i.e. vapor vs. liquid phase at the same density) in various single-collision and slowing-down distributions of sub-keV electron tracks in water. A unified methodology for both phases has been developed based on elements of the Born and Bethe theories which are used to establish inelastic cross-sections for energy loss. The linear dielectric response theory was used for the valence shells of the liquid phase together with Born-corrections at low energies. The methodology has been implemented in our Monte-Carlo code, MC4 [39], which performs full slowing-down simulation of electrons in an event-by-event mode and used for various track-structure calculations. Thereafter, the vapor-based version of the code will be denoted as MC4V, whereas, the liquid-based version as MC4L. All vapor results have been normalized to unit density.

3.2 Inelastic models

The first Born approximation (FBA) provides a suitable starting point for the description of the inelastic scattering process. The important result of this approximation is the factorization of the doubly-differential inelastic cross-section into a kinematic (projectile-dependent) and a dynamic (target-dependent) factor as follows [68]:

$$\frac{d^2\Sigma^{(1)}}{dE\,dQ} = \frac{8\pi\alpha_o^2 R^2 NZ}{T} \times \frac{S(q,E)}{Q^2} \tag{3.1}$$

where E is the energy-transfer, $Q=q^2/2m$ with q the momentum-transfer and m the electron rest mass, T is kinetic energy of the incident electron, α_o is the Bohr radius, R is the Rydberg constant, N is the molecular density, Z is the atomic number, and S(q,E) is the inelastic form-factor. According to common practice for condensed targets we use the macroscopic cross-section, Σ, also called the inverse mean-free-path, IMFP.

Equation (3.1) may be directly used for modeling the energy loss and angular deflection (i.e. momentum transfer) in an inelastic collision. In view, however, of the prominence of momentum transfer in elastic scattering, it is advantageous for an MC simulation to model the E-dependence directly from Bethe's asymptotic expansion. In accordance with the restrictions of the FBA, we keep only the first-order term and write the singly-differential cross-section as follows:

$$\frac{d\Sigma^{(1)}}{dE} = \left[A(E)\ln(T/R) + B(E) \right] T^{-1} \tag{3.2}$$

where $T=1/2mu^2$ (m: electron mass), and A(E), B(E) are target properties directly related to the form-factor. In particular, the A(E) depends on the optical-limit, S(q=0,E), whereas the B(E) relates to the full q-dependence of S(q,E). The difference between our vapor and liquid inelastic models lie solely in these two target-parameters, which have to be determined separately for the two phases of water. Since any phase effects would be limited to the valence shells, the core-shell

of water (i.e. the oxygen K-shell) is treated within the binary-encounter-approximation with exchange included [67].

3.2.1 Liquid phase

For the liquid phase, we take advantage of the following relationship between the form-factor and the loss-function:

$$S(q,E) = \frac{2}{\pi}\frac{Q}{E_p^2} Z \,\mathrm{Im}\left[-\frac{1}{\varepsilon(q,E)}\right] \tag{3.3}$$

where $\varepsilon(q,E)=\varepsilon_1+i\varepsilon_2$ is the complex dielectric-response function, E_p is the plasma energy of liquid water (21.6 eV), and $\mathrm{Im}(-1/\varepsilon)$ is the loss-function. It may then be shown that:

$$A(E) = \frac{1}{2\pi\alpha_o}\mathrm{Im}\left[\frac{-1}{\varepsilon(q=0,E)}\right] \tag{3.4}$$

Importantly the optical-loss-function in equation (3.4) may be determined from optical data by using the following relationship:

$$\mathrm{Im}\left[\frac{-1}{\varepsilon(0,E)}\right] = \frac{2nk}{\left(n^2-k^2\right)^2+\left(2nk\right)^2} \tag{3.5}$$

where n=n(E) and k=k(E) are the real and imaginary parts of the index of refraction, respectively, which have been experimentally measured for liquid water. A modified Drude expansion model has been used to analytically represent the

optical data consistent with the appropriate sum-rules. The following formula pertains to this model:

$$\varepsilon(0,E) = 1 + E_p^2 \sum_j \frac{f_j}{E_j^2 - E^2 - i\gamma_j E} \tag{3.6}$$

where the E_j, f_j, and γ_j are the adjustable model parameters found from the analytic representation of the optical data. The details of this procedure may be found in [33].

On the other hand, the B(E) parameter formally relates to the q-dependence of the form-factor. We have examined various dispersion (q>0) models for calculating proton [37] and electron [32] inelastic characteristics in liquid water. Here, we use the extended-Drude model as first suggested by Ritchie and co-workers [116]. The loss-function may then be calculated from:

$$\mathrm{Im}\left[\frac{-1}{\varepsilon(q,E)}\right] = \frac{\varepsilon_2(q,E)}{\varepsilon_1^2(q,E) + \varepsilon_2^2(q,E)} \tag{3.7}$$

where the ε_1=Re[ε(q,E)] and ε_2=Im[ε(q,E)] are now found from equation (3.6) under the substitution $E_j(q)=E_j+q^2/2m$, in accordance with the impulse approximation (restricted to the continuum), and $f_j=f_j(q)$, in accordance with an empirical generalized-oscillator-strength formula. We may then determine the B(E) by numerically integrating equation (3.1) and solving equation (3.2). For the continuum, we also account for the binary limit at large E by means of the binary-encounter-approximation. The details of this procedure are discussed in Chapter 2.

Perturbation corrections were included by means of a second-order term:

$$\frac{d\Sigma^{(2)}}{dE} = -\frac{2}{\pi\alpha_o T}\,\mathrm{Im}\left[\frac{-1}{\varepsilon(E,0)}\right] L(E). \tag{3.8}$$

Equation (3.8) was based on a classical impact-parameter perturbation calculation where the L(E) function depends on the cut-off distance that distinguishes between close and distant collisions in the calculation [4]. This function, however, becomes negative below about 100 eV. Therefore, a simple Coulomb-field correction [125] was adopted at lower energies which results in the substitution of T by $T+I_j+U_j$, where I_j and U_j are the binding and kinetic energy, respectively, of an electron at the j-th orbital. An exchange correction term was applied to the continuum by analogy to the Mott formula:

$$\frac{d\Sigma_j^{(ex)}(W,T)}{dW} = \frac{d\tilde{\Sigma}_j(T-W-I_j,T)}{dW} - \left[\frac{d\tilde{\Sigma}_j(W,T)}{dW}\times\frac{d\tilde{\Sigma}_j(T-W-I_j,T)}{dW}\right]^{1/2} \tag{3.9}$$

where W is the kinetic energy of the secondary electron ($W=E-I_j$), and

$$\frac{d\tilde{\Sigma}_j}{dW} = \frac{d\Sigma_j^{(1)}}{dW} + \frac{d\Sigma_j^{(2)}}{dW} \tag{3.10}$$

3.2.2 Vapor phase

For the vapor phase, we use the relationship between the form-factor and the oscillator-strength of the molecule:

$$S(q,E)=\frac{Q}{E}\frac{df(q,E)}{dE} \tag{3.11}$$

where df(q,E)/dE is the generalized-oscillator-strength (GOS). The A(E) may then be found from:

$$A(E)=4\pi\alpha_o^2R^2N\frac{df(q=0,E)}{E\,dE} \tag{3.12}$$

where df(0,E)/dE is the optical-oscillator-strength (OOS) which may be obtained from:

$$\frac{df(0,E)}{dE}=\left(4\pi^2\alpha\alpha_o^2R\right)^{-1}\sigma_{ph} \tag{3.13}$$

where α is the fine structure constant and σ_{ph} the photo-absorption cross-section. The analytic determination of the OOS for the water molecule based on experimental σ_{ph} data has been given in [35].

The B(E) for the vapor is found directly from equation (3.2) by using the experimental inelastic cross-section data at the limited incident energies available. However, since, formally, the B(E) is independent of T, it may then be used at any incident energy. Similar to the liquid case, the binary-encounter-approximation (with an exchange correction) was used as an asymptotic limit of equation (3.2) for the continuum. Any further low-energy Born corrections are automatically incorporated in the empirical derivation of B(E), since the available cross-section data for the vapor go down to a few tens of eV. The procedure is discussed in more detail in [35].

3.3 Angular deflections

Data on the angular distribution of electrons in liquid water following an elastic or inelastic collision do not exist. As a result, and in view of the difficulties associated with the theoretical treatment of this problem, a methodology applied earlier to the vapor phase has been adopted here for both phases. In view of other uncertainties, this is a reasonable approximation. In summary, the screened-Rutherford formula with Moliere's screening parameter has been used for the total elastic, as well as, for the differential above 200 eV. At lower energies empirical distributions were used [17]. The angular distributions of the scattered and secondary electrons after ionization were obtained based on the kinematics of binary collisions and the data of Opal and co-workers as described in [51].

3.4 Results

In Figure (3.1a), (3.1b) we present secondary electron spectra for electron ionization collisions in vapor and liquid water for two characteristic incident energies, namely, for 1 and 0.1 keV. The liquid results have been calculated by the FBA (a first-order perturbation theory), the FBA supplemented by a second-order term plus an exchange correction, as well as, by the simple Mott formula modified by the binding energies of liquid water. It may first be seen that corrections to the FBA are unimportant at 1 keV (the two plots are indistinguishable in Figure (3.1a)),

becoming of the order of 50% at the peak (W≈10 eV) of the 0.1 keV distribution (Figure (3.1b)). It is also evident that the vapor spectra are notably different from the liquid spectra. At both energies the liquid spectra are harder; the most probable secondary energy is about 10 eV for the liquid whereas it is only 2-3 eV for the vapor. This is due to an upward shift of the oscillator-strength in the condensed phase resulting from inter-molecular bonding [133]. The Mott calculations fail to reproduce the proper shape of the secondary spectra, especially at the low-energy range where the binary approximation fails. As expected, all distributions come together at high secondary energies where the details of electronic structure become gradually less important.

In Figure (3.2) we present the inelastic IMFP from 10 keV down to threshold. Regarding phase-effects the following conclusions follow: (i) Differences between the two phases become noticeable below 1 keV, since the binary character prevails at higher impact energies; (ii) The vapor IMFP is by a factor of 1.4 higher than the liquid at 100 eV, due to screening effects in the condensed phase; (iii) The vapor IMFP peaks at lower impact energies (~70 eV) compared to the liquid (~120 eV), due to the upward shift of the oscillator-strength in the condensed phase; (iv) The correction terms to the FBA appear to be important below 1 keV, especially since the magnitude of the correction is of the same order as the vapor-liquid difference.

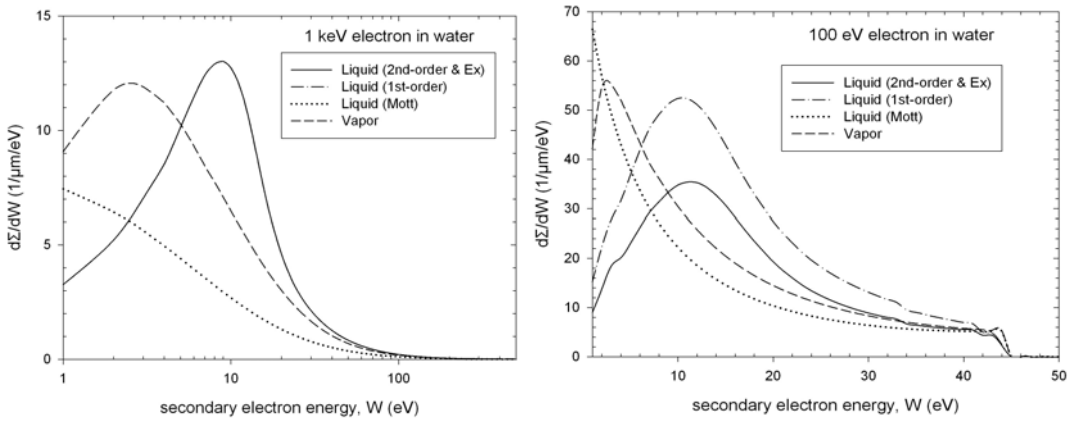

(a) (b)

Figure 3.1. Secondary electron spectra for electron impact in the two phases of water calculated by various inelastic models: (a) 1 keV electron impact; (b) 0.1 keV electron impact.

Nevertheless, the screening and upward shift in the liquid is still evident in the FBA results. As expected, the Mott-calculated IMFP is way off throughout most of the depicted energy range, a direct consequence of the failure of the binary approximation in the low-energy range.

In Figure (3.3) the dependence of the mean energy loss, $<E_{loss}>$ per collision on incident electron energy is shown. In relation to previous discussion, it may be clearly seen in this Figure that the harder collision spectrum in the liquid phase results in a larger mean value than in the vapor by about 5 eV. A binary approximation, on the other hand, results in even larger differences as the Mott results indicate.

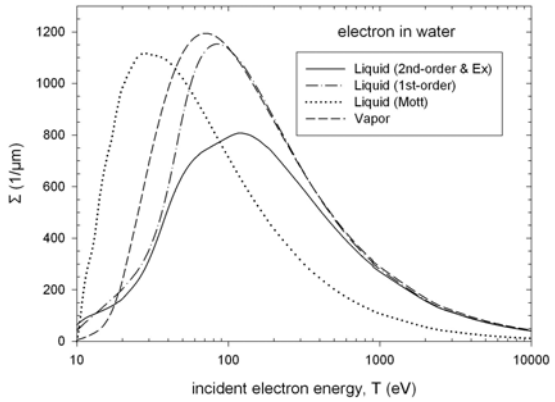

Figure 3.2. Electron inelastic inverse-mean-free-path (IMFP) for the two phases of water calculated by various inelastic models.

In the following Figures we present and compare MC calculations from full slowing-down electron tracks (followed down to 1 Ry) from the MC4V and MC4L versions. Here Ry denotes the Rydberg energy which is defined as the binding energy of the electron in the hydrogen atom (13.6 eV).

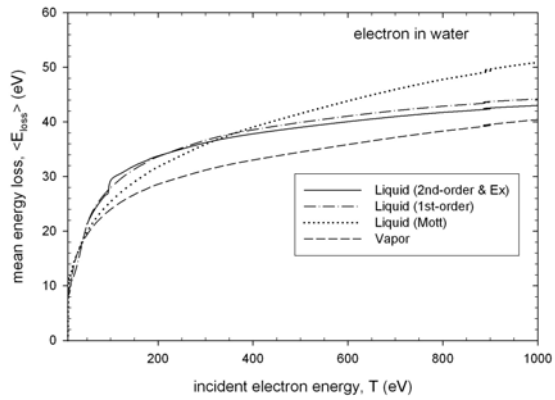

Figure 3.3. Average energy loss as a function of incident energy for electron inelastic impact in the two phases of water calculated by various inelastic models.

Figures (3.4a), (3.4b) present distributions of absorbed energy (per track) in spherical shells at 1 nm radial intervals from the point of origin of monoenergetic electron sources of 0.1, and 1 keV initial energies. To obtain reasonable statistics, the results are averaged over 1000, and 10000 electron tracks, respectively. Although the liquid distributions do appear to have a slightly smaller spread-out pattern (rise higher and peak earlier) than the vapor ones at the 1 keV energies, the effect is much smaller than previously considered [102]. In particular, these results reveal that the screening effect, which is responsible for larger MFPs in the liquid, is almost equally compensated by the effect of the hardening of the liquid spectrum (larger $<E_{loss}>$), which acts in the opposite direction resulting in the dissipation of energy closer to the origin. Interestingly, this pattern is reversed at very low energies (the 100 eV case) where the screening effect seems to be more important than the hardening effect, i.e. it is the MFP and not the $<E_{loss}>$ which governs the distribution. This is reasonable, in view of the much smaller number of collisions during slowing-down at this incident energy. The above arguments are further supported by the behavior of the FBA-based distributions. Here, the effect of screening is minimal (the MFP is very close to the vapor), whereas the hardening is still in effect. As a result, the 100 eV distribution is very close to the vapor, whereas the higher energy distributions show a smaller spread-out pattern. The Mott-based distributions may be explained by the same arguments.

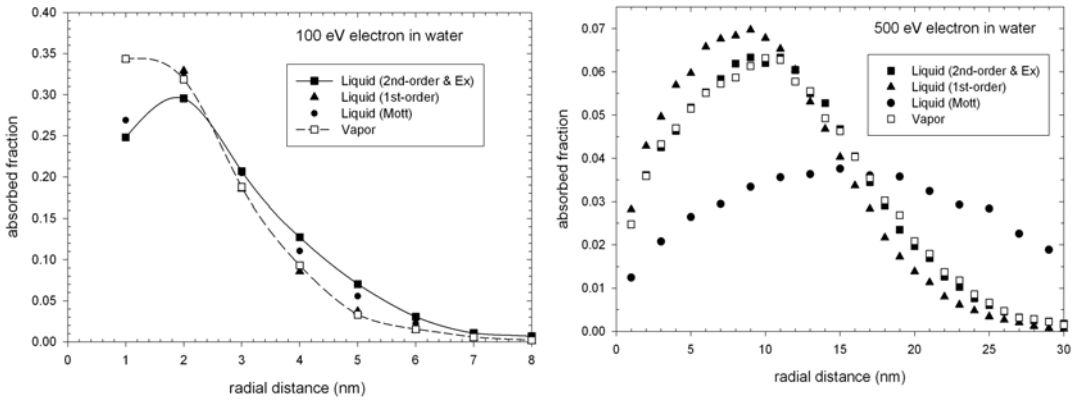

(a) (b)

Figure 3.4. Monte-Carlo calculated radial distribution of absorbed fraction in spherical shells of 1 nm intervals centered at the electron-track origin in the two phases of water. The initial electron energy was: (a) 0.1 keV (the two lines are to guide the eye), (b) 1 keV.

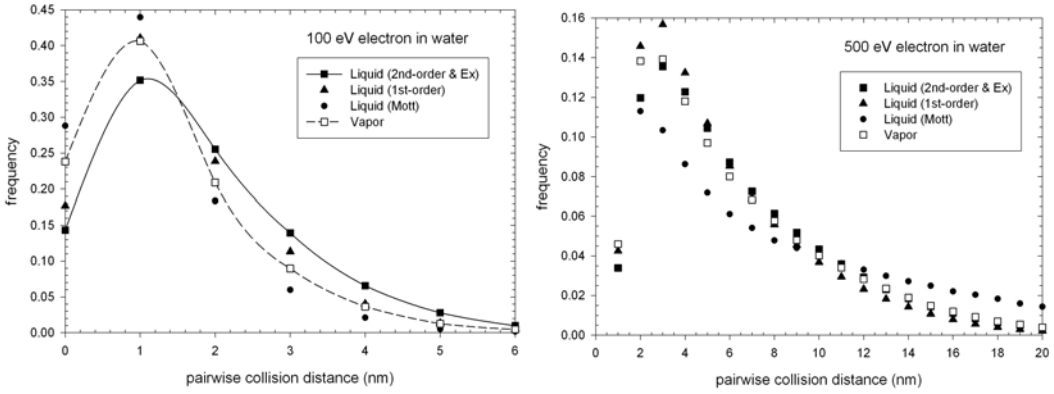

(a) (b)

Figure 3.5. Monte-Carlo calculated frequency distribution of distances between inelastic collisions in full slowing-down electron tracks in the two phases of water. The initial electron energy was: (a) 0.1 keV (the two lines are to guide the eye), (b) 1 keV.

Although the pattern of energy deposition as presented, for example, in Figure (3.4), provides important information on track-structure characteristics,

biological damage is largely the result of clustering of events in critical cellular structures. One of the most basic clustering characteristic is the probability distribution of distances between two inelastic collisions. Such distribution provides also important information for the subsequent chemistry. In Figure (3.5a), (3.5b) we present such distributions at three different initial electron energies calculated on the basis of the same inelastic models as in Figure (3.4). At all energies, the distribution peaks at about 1-3 nm distances which is of particular significance considering that 2 nm is the diameter of the DNA double helix. As the electron increases, the tail of the distribution increases due to the larger MFPs involved. The vapor distributions peak at the same distances with the liquid (the corrected-FBA results) but higher due to the larger IMFP in the vapor phase (see Figure (3.2)) which results in smaller distances between successive collisions. The reason that the FBA distributions of the liquid peak even higher than the vapor, although the respective IMFPs are somewhat lower (see Figure (3.2)), is due to the more efficient dissipation of energy in the liquid, which, in turn, is the result of the higher $<E_{loss}>$.

Chapter 4

Monte-Carlo calculations of radial dose and restricted-LET for protons in water

4.1 Introduction

The microscopic distribution of deposited energy around proton tracks is of importance for assessing and modeling radiation effects from neutron and/or ion beams in materials. Such knowledge has been widely applied in radiation biophysics, radiation detector physics, and solid-state microelectronic devices [121].

An important aspect of ion track analysis with respect to radiation action is the energy deposited “locally”, that is, at restricted regions around the ion path. To that end, a basic, yet very practical, quantity is the ion’s radial dose profile which is defined as the distribution of the average energy density deposited in co-axial cylindrical shells around its axis. Due to symmetry, the distribution of events

around any given track-segment would only be a function of the radial distance, whereas, due to the dependence of the inelastic cross-section on the ion's velocity, the radial profile would change along the track axis. A related quantity that perhaps more directly quantifies the energy deposited within certain distances from the ion's path is the spatially-restricted linear-energy-transfer (LET). It may be obtained from the radial dose profile by integration up to a specified radial cut-off. It is well known that the spatially-restricted LET represents more accurately the deposited energy in restricted domains around the ion's path than the conventional energy-restricted LET (i.e. with an energy-loss cut-off) and, therefore, it is more suitable for describing measurable quantities [75].

Experimental investigation of radial profiles for condensed targets, however, are difficult and, as a consequence, great emphasis has been put on theoretical studies which are either of analytic nature or based on Monte-Carlo (MC) simulation [2]. In the former, the integral which defines the radial dose distribution is computed numerically on the basis of some analytic electron transmission probability functions or, as done originally, it is numerically solved by introducing a simple energy-loss model [23]. MC simulations, apart from their complexity, offer the distinct advantage that the stochastics of the energy-loss processes are inherently accounted for, providing a more realistic description of the variation of the secondary slowing-down spectrum with radial distance. In fact, MC results may be used to obtain electron transmission functions for subsequent use in numerical calculations of radial profiles. The above discussion applies also to the

spatially-restricted LET since, in contrast to its energy-restricted counterpart, which may be formally evaluated from the single-collision spectrum; the use of a radial cut-off prohibits an analytic calculation.

In the present work, MC calculations of radial dose profiles and spatially-restricted LET are presented based on two recent versions of our previously developed MC code for water (MC4W) [36, 35] which transports in an event-by-event mode non-relativistic light ions (with ion charge $z<10$) above about 0.5 MeV/amu, and electrons down to the ionization threshold (~1 Ry). The particle-water interaction models implemented in the initial MC4W code were based on the so-called gas-phase approximation. In subsequent studies the physics models used in MC4W were improved and also extended to the liquid phase using the dielectric approach which directly accounts for condensed-phase effects pertaining to liquid water [38, 41, 32]. Thereafter, the latest version of the code pertaining to the vapor phase will be denoted as MC4V, whereas, the one developed for liquid water as MC4L.

4.2 Physics input

4.2.1 Energy-loss models

For non-relativistic and sufficiently fast projectiles, the Bethe theory [68] provides a consistent theoretical framework for modeling the entire single-collision

energy loss spectrum, that is, both soft- and hard-collisions. Note that all classical collision models fail to properly account for the production of low-energy electrons by soft-collisions which are of great importance for accurate track-structure calculations [67]. Therefore, the modeling of inelastic interactions (i.e. ionizations and excitations) is based on Bethe's asymptote, the first-order term of which may take the following form for the macroscopic differential cross-section [68]:

$$\frac{d\Sigma}{dE} = \left[A(E) \ln(T/R) + B(E) \right] T^{-1} \tag{4.1}$$

where E is the energy loss, $T=mv^2/2$ (m: electron mass; v: projectile velocity), and A(E), B(E) are target properties independent of the projectile. In equation (4.1), higher-order terms are neglected since they are generally beyond the range of applicability of Bethe's theory. In essence, the difference between the MC4V and MC4L versions lies solely in A(E) and B(E), which have to be determined separately for the vapor and liquid phases of water (see below). The nature of these parameters is revealed by considering the behavior of equation (4.1) in the limits of soft and hard collisions:

$$\left.\frac{d\Sigma}{dE}\right|_{soft} \approx A(E) T^{-1} \ln(T/R) \tag{4.2}$$

$$\left.\frac{d\Sigma}{dE}\right|_{hard} \approx B(E) T^{-1} \tag{4.3}$$

It then follows that A(E) governs the spectrum of soft-collisions and is related to the optical absorption spectrum of the target, which is experimentally

available for many materials including both vapor and liquid water. On the other hand, B(E) is associated with hard collisions and relates to the entire Bethe-surface. In view of the difficulties associated with the determination of B(E) theoretically, the following semi-empirical scheme was adopted.

For ionizations, the methodology of Miller [86] was applied to the four outer-shells of water, which are largely responsible for phase-effects. The cross-section differential in the secondary electron energy, W (=E_j-I_j where I_j is the binding energy in the j-th orbital) is written as:

$$\frac{d\Sigma}{dW} = \frac{d\Sigma_{soft}}{dW} + B'(W)\frac{d\Sigma_{hard}}{dW} \tag{4.4}$$

where the function $B'(W)$, which takes values in the unit interval, moderates the contribution of hard collisions and, therefore, is related to the B(E) of Bethe's theory. Although various models are available for the hard-collision component, the binary-encounter theory was adopted here, since it may be shown to follow as a high-E approximation to Bethe's theory and, therefore, provides a consistent extension of the present model to hard collisions [68].

In the MC4V version, the function $B'(W)$ was determined by adjusting equation (4.4) to the available experimental cross-section data for the vapor, whereas the A(E) function entering the soft-collision term (see equation (4.2)) was determined from optical data using the relationship:

$$A(E) \sim \frac{1}{E}\frac{df}{dE} \tag{4.5}$$

where df/dE is the optical-oscillator-strength density of the water molecule. The latter is experimentally determined from photoionization data. Note that the soft-collision component used in the above methodology (see equation (4.2)) is somewhat different from the one used in the initial MC4W code. The present treatment is preferable since it avoids the negative contribution of the logarithmic term of the previous model for sufficiently high W. Furthermore, from a Platzman plot [77, 76] analysis it has been found that the experimental cross-section data of the vapor do not follow the theoretically correct behavior at small energy losses where the A(E) term should be dominant [41]. This inconsistency must be due to the large experimental uncertainties accompanying the detection of secondaries with extremely small kinetic energies (W<10 eV) [67]. It was, therefore, decided to further improve the model used in MC4W and to adopt the condition B'(W<10 eV)=0 in the recent MC4V version.

In the MC4L version, on the other hand, and in the absence of experimental cross-section data for the liquid phase, equation (4.4) was adjusted to data calculated using a dielectric model of the Bethe-surface of liquid water which has been successfully applied to both proton and electron inelastic interactions [38, 41, 32]. The A(E) function in this case was also obtained from available optical data by means of the relationship:

$$A(E) \sim \mathrm{Im}\left[\frac{-1}{\varepsilon(E)}\right] \tag{4.6}$$

where ε(E) is the complex dielectric-response-function of liquid water, which may be determined experimentally from reflectance measurements.

For oxygen K-shell ionization (i.e. the inner-most shell of water) it is sufficient to simply use the binary-encounter theory. The separate treatment of valence and core shell electrons of water may be justified by the large difference in their binding energies (>500 eV). In particular, the neglect of collisions with small momentum transfer (i.e. the soft-collision contribution) in the binary-encounter treatment of the K-shell electrons is a reasonable approximation in view of the large binding energy that needs to be overcome. Therefore, in both MC4V and MC4L, proton-impact K-shell ionization was treated by the BEA formula [67], whereas, for electron-impact an exchange and Coulomb-field corrected formula (named BEAX by ICRU [67]) was used. In contrast to the initial MC4W code, Auger emission after K-shell ionization is included in both new versions assuming isotropic emission.

For excitations, the parametric representation of the discrete spectrum was established by writing Bethe's first-order term (see equation (4.1)) in the form:

$$\Sigma_j = A_j T^{-1} \ln\left(C_j \frac{T}{R} \right) \tag{4.7}$$

where C_j is related to the Bethe parameters by means of $\ln[C_j] \approx B_j/A_j$. Following the suggestion of Green and co-workers [52] the analytic representation was substantially improved by the introduction of an "adjusting" function which operates at low-energies and has the form $[1-(X_j/T)]^{pj}$ where X_j is the transition

energy. Note that equation (4.7) is a somewhat simplified version of the one used in the initial MC4W code. The parameters A_j, C_j, P_j in MC4V were determined by fitting the available experimental data for the eight discrete transitions of the molecule, whereas, in MC4L, they were determined by fitting the calculated dielectric cross-section data for the five discrete transitions of the liquid phase.

4.2.2 Electron low-energy corrections

At energies where the incident electron may no longer be considered as fast as compared to the target electrons with which it interacts, the Bethe theory is known to gradually overestimate the cross-section and, eventually fail, since it is a first-order perturbation theory. Thus, for energies below a few hundred eVs, it is necessary to provide corrections due to higher-order perturbation terms and to the indistinguishability between the impact and ejected electrons.

In MC4V, low energy corrections have been automatically provided by fitting the low-energy experimental data, which, by default, include such effects. To facilitate an accurate representation of the data, however, it was found advantageous to use in equation (4.4) the corrected-BEA formula (i.e. the BEAX) for the hard-collision component, whereas, as already noted, a low-energy adjusting function was also included in equation (4.7) for the excitations. In contrast to the initial MC4W code, however, the condition $B'(W<10\ eV)=0$ adopted in MC4V resulted in a total ionization cross-section in better agreement with the experimental data, thus, avoiding the normalization function used in the initial version.

In MC4L, perturbation corrections were accounted for by the inclusion of a second-order term which reads as follows [131]:

$$\frac{d\Sigma^{(2)}}{dE} = -\frac{2}{\pi\alpha_o T}\,\mathrm{Im}\left[\frac{-1}{\varepsilon(E,0)}\right] L(E) \tag{4.8}$$

where α_o is the first Bohr radius. equation (4.8) has been derived from a classical impact-parameter perturbation calculation where L(E) is a function which depends on the cut-off distance that distinguishes between close and distant collisions in the calculation. equation (4.8), however, is inadequate at the lowest energy range (below about 100 eV) because the function L(E) becomes negative for certain values of E. A simple Coulomb-field correction was therefore adopted for T<100 eV similar to the one used in the BEAX formula. The exchange correction term applied only to ionizations was obtained by analogy to the Mott formula [131]:

$$\frac{d\Sigma_j^{(ex)}(W,T)}{dW} = \frac{d\Sigma_j(T-W-I_j,T)}{dW} - \left[\frac{d\Sigma_j(W,T)}{dW}\times\frac{d\Sigma_j(T-W-I_j,T)}{dW}\right]^{1/2} \tag{4.9}$$

where each term in equation (4.9) should be understood as applied to the sum of the first- and second-order term of the differential ionization cross-section (Equations (4.4) and (4.8)).

4.2.3 Angular deflections

Due to the lack of available data on the angular distribution of electrons in liquid water following an elastic or inelastic collision, and in view of the theoretical difficulties associated with this problem, the methodology used in the initial MC4W vapor code was also adopted for the liquid. In view of other uncertainties, this is a reasonable approximation which has also been adopted in many other liquid water codes.

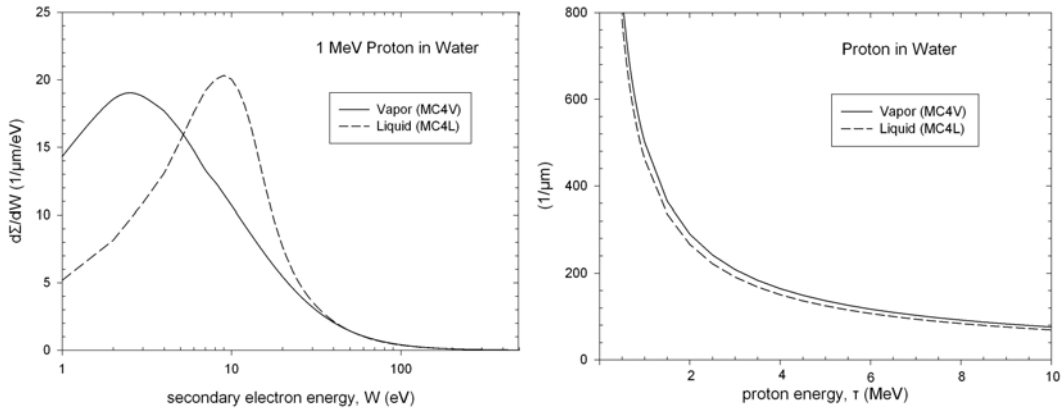

(a) (b)

Figure 4.1. Proton inelastic macroscopic cross-sections for the two phases of water: (a) secondary electron spectrum for 1 MeV protons; (b) inverse mean free path.

To summarize, the screened-Rutherford formula with Moliere's screening parameter was used for the total elastic cross-section as well as for the differential above 200 eV. At lower energies the empirical distributions of Brenner and Zaider [17] were used. The angular distributions of the scattered and secondary electrons

after ionization were obtained based on the kinematics of binary collisions and the data of Opal et al. [107] as described by Grosswendt and Waibel [51].

4.3 Results

The differences in the physics implemented in the MC4V and MC4L versions are shown in Figures (4.1a), (4.1b) and (4.2), where the differential and integrated inelastic cross-sections for the two phases of water are compared for both protons and electrons. (The electron differential distributions have been omitted since they exhibit exactly the same trends with the protons of the same velocity.) Both kinds of distributions are essential in an MC simulation; the integrated is the inverse mean free path for inelastic collisions, whereas, the differential determines the energy of the secondary electron after an ionization event. Figure (4.1a) shows that in MC4V there is an increased chance of secondary emission at threshold energies (at just a few eVs), whereas, in MC4L, most secondaries will be emitted with energies around 10 eV, which is consistent—given the binding energies of the valence shells—with the peak of the optical absorption spectrum of the liquid at about 22 eV. In terms of the integrated distributions, protons seem to be fairly indifferent to the phase of the medium (see Figure (4.1b)), due to the large upper limit of integration over W which compensates the differences observed in Figure (4.1a) at small W. In contrast, significant differences are observed for electrons below a few hundred eVs where phase-effects

influencing the soft-collision spectrum become decisive. Therefore, in MC4V electrons of very low energies have smaller mean-free-paths (≡1/Σ) compared to MC4L. The uncorrected (i.e. first-order) results for the liquid are also depicted in Figure (4.2) for comparison. Interestingly, the magnitude of the correction appears to be comparable to the differences observed between the two phases.

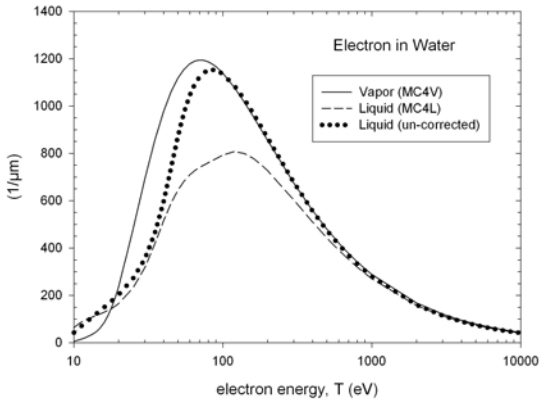

Figure 4.2. Electron inelastic inverse mean free path for the two phases of water. Dotted curve is without the low-energy corrections (see text).

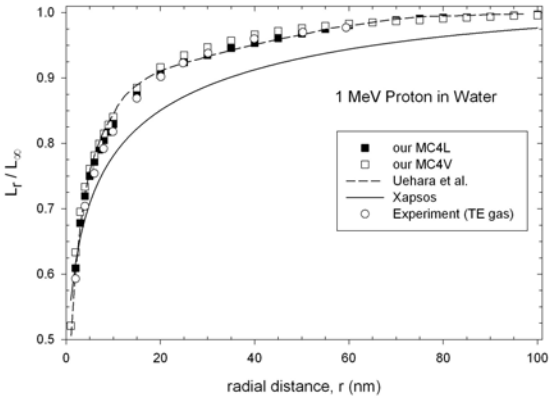

Figure 4.3. Ratio of radially-restricted to unrestricted stopping-power for 1 MeV protons calculated by the present codes for the two phases of water and compared to other studies.

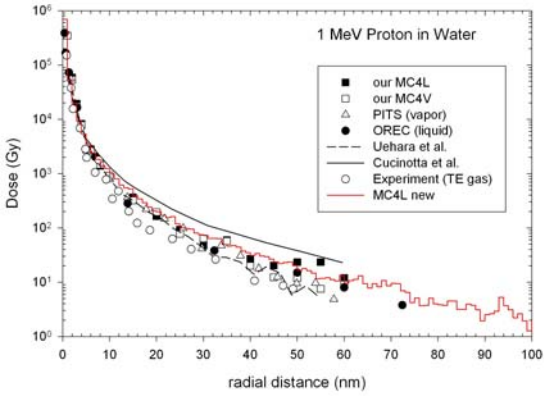

Figure 4.4. Radial dose profiles for 1 MeV protons calculated by the present codes for the two phases of water and compared to other studies.

In Figure (4.3), radial dose distributions for a 1 MeV proton calculated by both MC4V and MC4L are depicted. The results have been obtained by scoring the energy deposition from secondary electrons at cylindrical shells at 1 nm radial intervals. For obtaining reasonable statistics, the results are averaged over 10000 proton track segments. Note that the energy deposition by the proton itself has been excluded for allowing a meaningful comparison with other studies. For both phases, its contribution is about half the energy deposited in the first shell by the secondaries. Comparison is made with the old experimental data for tissue-equivalent gas [148], the MC results from the OREC liquid code [55] and the PITS vapor-water code [143], the more recent simulation data of Uehara et al. [137], as well as, the more recent theoretical calculations of Cucinotta et al. [23]. Analytic formulae have also been obtained by Chen et al. [21], Chen and Kellerer [20], and Grosswendt and Baek [26]. Despite the variety of methods (experimental, theoretical/analytical, simulation) used to obtain the various data depicted, they are

all within reasonable agreement to each other. Furthermore, no marked differences between the results of the MC4V and MC4L versions are observed.

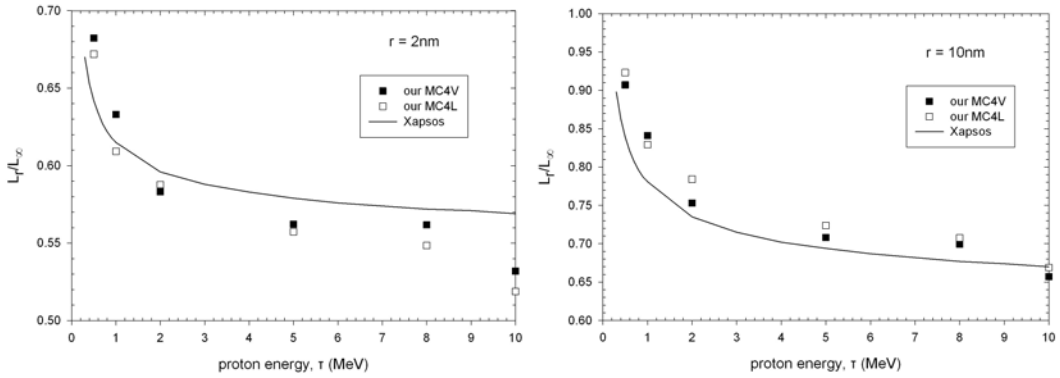

(a) (b)

Figure 4.5. Fraction of a proton's energy loss deposited within (a) 2nm and (b) 10 nm track radius, for various proton energies calculated by the present codes for the two phases of water and compared to an analytic model.

Radius (nm)	0.5 MeV		1 MeV		5 MeV	
	Vap	Liq	Vap	Liq	Vap	Liq
r=5	37.0	36.7	21.2	20.7	5.00	5.07
r=10	40.8	40.4	23.4	22.9	5.42	5.52
r=20	43.8	43.0	25.5	25.0	5.88	5.97
r=50	44.9	43.8	27.2	26.7	6.41	6.57
r=100	45.0	43.8	27.7	27.5	6.72	6.88
r=∞	45.0	43.8	27.9	27.6	7.65	7.63
ICRU [66]	42.0	41.3	26.4	26.1	7.98	7.91

Table 3. Radially-restricted LET in eV /nm for protons of various energies in water (Vap=vapor, Liq=liquid, ICRU=unrestricted LET).

Spatially-restricted LET (L_r) values for selected proton energies calculated by the MC4V and MC4L versions are presented in Table 1, along with the ICRU

[189] values for the electronic stopping-power (i.e. the un-restricted LET, L_∞). The differences with ICRU are less than 8%. In Figure (4.3), the fraction of the proton's energy loss (i.e. the ratio of the restricted LET to the unrestricted LET, L_r/L_∞) is depicted as a function of the radial distance from the proton's track axis. In addition to the results from the studies presented in Figure (4.4), calculations based on the analytic model of Xapsos [151] are also shown. Despite its simplicity, Xapsos model is in fair agreement with the more elaborate MC calculations. For radiobiological applications and, in general, for modeling radiation action in materials, it is often of interest to know the energy deposited "locally", that is, within a short distance from the ion's path as it traverses a sensitive target. Since the latter is often of nanometer dimensions, the fraction of the proton's energy loss deposited within 2 and 10 nm from its axis is presented in Figures (4.5a), (4.5b) for various proton energies. The particular dimensions selected correspond to the diameters of DNA and nucleosome, respectively. The reduction of L_r/L_∞ with increasing proton energy is caused by an increasing fraction of energetic δ-rays produced by knock-on collisions of protons. The maximum energy of these δ-rays is proportional to the proton energy ($W_{\delta,max} \approx 4T_{proton}/1836$) and, thus, as the latter increases, a smaller fraction of the electron energy is deposited locally. In conclusion, overall, Xapsos analytic method compares well to our MC calculations (<15%), whereas, phase-effects (i.e. vapor vs. liquid water) appear to have small impact on radial dose profiles and restricted-LET for protons in the examined energy range (<10%).

Chapter 5

A Monte-Carlo study of energy deposition by heavy charged-particles in sub-cellular volumes

5.1 Introduction

It is generally recognized that an accurate description of energy deposition in sub-cellular targets ranging from a few to few hundreds nanometers will be necessary for a mechanistic understanding of radiation effects in cells [49]. Such information will also provide a more realistic physical input to current biophysical models which will eventually lead to more accurate predictions of the relative biological effectiveness of various ionizing particles relevant to cancer therapy and protection [108]. Furthermore, it is reasonable to expect that as biophysical techniques are becoming capable of reliably identifying cellular damage at the single-molecule level, the level of accuracy of the physics input will start to practically matter.

At the sub-cellular level, the pattern of energy deposition may be extremely non-uniform [101]. Thus, given the non-linear response of most biological systems to elementary events, a meaningful quantification at this spatial scale will have to entail the associated statistical fluctuations (straggling). Along with efforts to obtain such information experimentally [53], the conventional approach takes advantage of the unique capabilities of the so-called detailed-history Monte-Carlo (MC) codes which simulate each particle track (history) in full detail, that is, following all inelastic and elastic interactions event-by-event [104]. This is in contrast to the general-purpose condensed-history MC codes, like MCNP, EGS, GEANT, FLUKA, and PENELOPE, which group together several collisions into an artificial macroscopic step and simulate each particle track in a step-by-step mode [95]. Thus, sub-cellular dosimetric calculations are beyond the resolution capabilities of condensed-history codes.

In the present work, our in-house detailed-history code MC4 is used to obtain energy deposition and straggling distributions for sub-cellular volumes as a function of the impact geometry and the size of the volume. Specifically, protons and alpha particles of 0.5, 1, and 5 MeV/amu passing through or near spherical volumes ranging from 2-200 nm in diameter are considered. Secondary electron transport is explicitly accounted for so that both the energy that escapes by δ-rays created within the site and energy that enters from δ-rays created outside the site is considered. The results are obtained with two different versions of MC4; namely, the original vapor version [35] (of unit density) and the most recent liquid version

which is based on an improved dielectric model for liquid water [40]. The latter is based on an accurate parameterization of the whole Bethe surface obtained experimentally by inelastic X-ray scattering (IXS) spectroscopy [142, 57]. Therefore, the present liquid version updates the earlier version (see Chapter 2) which was based on a much less accurate set of optical data [58] and simple assumptions about dispersion [42]. A brief review of the cross-section input with emphasis on recent refinements is first presented.

5.2 Method

Total and differential inelastic cross-sections for the electronic energy loss of charged particles in both the vapor and liquid phases were constructed based on a parameterization of Bethe's asymptotic expansion as suggested by Miller *et al* [87]. This method has also been used in the ion codes PITS [143] and that of NIST [10]. The first-order term of Bethe's asymptotic expansion may be expressed as a function of two coefficients [68]:

$$\frac{d\Lambda}{dE} = T^{-1}\sum_i \left[A^{(i)}(E)\ln(T/R) + B^{(i)}(E) \right] \tag{5.1}$$

where Λ is the inelastic inverse mean free path, E is the energy transfer, $T=mv^2/2$ (m: electron mass; v: projectile velocity), and $A^{(i)}(E)$, $B^{(i)}(E)$ are coefficients characteristic of the i-th electronic transition. Their values depend on the atomic composition and state of condensation of the target. In essence, the main difference

between our vapor and liquid models lies on the algorithm used to determine these two coefficients. The *A* coefficient describes the electronic energy loss spectrum of the target at the optical limit (~zero momentum transfer) and, therefore, determines the soft collision contribution. For the vapor we use the relationship:

$$A_{vap}^{(i)}\left(E\right) \sim \frac{1}{E}\frac{df_{vap}^{(i)}\left(E,q=0\right)}{dE} \tag{5.2}$$

where *df(E,0)/dE* is the optical oscillator strength of the H_2O molecule. The latter was determined from photoabsorption data of the vapor phase [35]. For the liquid we use the dielectric formulation where condensed-phase effects are build into the formalism through the magnitude of the real and imaginary parts of the dielectric response function:

$$A_{liq}^{(i)}\left(E\right) \sim \mathrm{Im}\left[\frac{-1}{\varepsilon^{(i)}\left(E,q=0\right)}\right] = \frac{\mathrm{Im}\left[\varepsilon^{(i)}\left(E,0\right)\right]}{\left|\varepsilon\left(E,0\right)\right|^2} \tag{5.3}$$

where ε(*E*,*q*=0) is the optical dielectric response function of liquid water obtained from IXS data at *q*≈0 [40].

On the other hand, the *B* coefficient accounts for non-dipole transitions associated with hard collisions. Thus, its magnitude is determined by the *q*-dependence of the oscillator strength or the dielectric function. In the present implementation, the analytic evaluation of the *B* coefficient takes advantage of the following two properties: (i) its independence from *T*, and (ii) its asymptotic limit at large *E*. By solving equation (5.1) we obtain:

$$B^{(i)}(E) = T\frac{d\Lambda^{(i)}}{dE} - A^{(i)}(E)\ln(T/R) \tag{5.4}$$

For the vapor, the first term on the left-hand-side is obtained by the available experimental cross-section data for the individual discrete transitions and the total ionization probability [35]. The relevant cross-section data are not available for the liquid. Thus, we have undertaken numerical dielectric calculations to obtain the $d\Lambda^{(i)}/dE$ (for ionization) and $\Lambda^{(j)}$ (for excitation) of liquid water channel-by-channel [40].

The present implementation offers the following improvements over previous versions. For the vapor, the asymptotic behavior of the *B* coefficient, which determines the knock-on δ-rays, has been refined so as our stopping power values converge to within 1% to the ICRU values at 10-20 keV. For the liquid, both coefficients have been determined on the basis of more recent dielectric data for liquid water [142, 57]. In particular, we have implemented our new dielectric model which, contrary to the earlier used model [32, 27], provides an improved representation of the experimental Bethe surface over the whole *E*-*q* plane [40]. A weak point in our methodology is that, in the absence of a realistic band structure model for liquid water, the partitioning of the dielectric function to the various inelastic channels is obviously tentative. Nevertheless, an important aspect of the new liquid version is that, within the uncertainty of the dielectric data (few %) and for not too low projectile energies, the differential and total inelastic cross-sections (summed over all channels) used is almost “exact”. Thus, the above methodology

provides a self-consistent and experimentally motivated scheme for constructing (non-relativistic) inelastic cross-sections in the range where the Bethe and Born theories are valid; that is, for protons and alpha particles above ~0.5 MeV/amu and secondary electrons above ~0.3 keV. For treating the low energy secondaries down to threshold (~1 Ry) perturbation and exchange correction terms need to be applied. For the vapor such corrections have been automatically included through the use of direct experimental cross-section data down to very low energies (~1 Ry). For the liquid, on the other hand, the first-order dielectric theory is corrected by the use of a Barkas-type second-order term and Mott-like Born-exchange terms as in the previous liquid version (see Chapter 2). Both terms, however, depend on the dielectric function so their present magnitudes differ from the earlier version. Finally, for both phases the same schemes have been used to model the angular deflections after elastic/inelastic scattering as described elsewhere [35]. They are based on a combination of experimental data for the vapor phase and binary collision theory. The justification for treating angular deflection in an identical manner for both phases is provided from the following observations: (i) there exists no data for electron elastic scattering in the liquid phase, and (ii) at the typical secondary electron energies (<100 eV) inelastic scattering contributes minimally to deflection as compared to elastic scattering; thus, a more elaborate treatment of inelastic scattering angles through the q-dependence of the dielectric functions would not make a noticeable difference.

Simulations have been performed for proton and alpha particle track segments of 1 μm length that were allowed to randomly overlap target spheres of various dimensions and of unit density. For reasonable statistics (few % uncertainty) calculations are averaged over 1000 projectile histories. Both the primary projectile and all its secondary electrons (hereafter called δ-rays irrespective of their energy) are simulated in a detailed-history mode based on the interaction cross-sections of both the vapor and liquid phases of water as described in the previous section. The δ-rays are individually followed down to 1 Ry. The stochastic energy imparted, ε, to the target volume is given by the sum $\sum_i \Delta\varepsilon_i$ where each $\Delta\varepsilon_i$ is either potential energy following an excitation or ionization event or the kinetic energy of a sub-cutoff electron that originate within the volume. Since we deal with specified track-target geometries it is more useful to divide ε by the site diameter, *d*, and not the mean chord length (=2/3×*d*). For example, *d* is still meaningful for projectiles passing outside the site and it also allows for a direct comparison with LET-based analytic calculations.

5.3 Results and discussion

Figure (5.1) presents the mean event size in volumes of 10 and 100 nm diameter for protons passing at various distances, *b*, from the center. To facilitate the comparison between different sites the results are presented as a function of the

normalized impact parameter b/r, where r is the sphere radius ($r=d/2$). Along with our MC simulation results for the two phases of water we also provide for comparison analytic calculations based on the (unrestricted) LET. The latter are obtained by the relationship: $\langle \varepsilon \rangle = 2\left(r^2 - b^2\right)^{1/2} \times LET$ which assumes that the mean energy loss by the proton is completed absorbed within the site; thus, both energy loss straggling and δ-ray effects are neglected. The present MC results are in good agreement with the ones obtained by MOCA [147] and more recently by PITS [103]. Several observations follow from Figure (5.1): (i) Since the majority of δ-rays are of very low energy (<100 eV) with penetration distances of the order of nanometers (<10 nm), differences between the LET-based and MC simulation results increase with decreasing sphere diameter. Specifically, the analytic calculations overestimate the simulated absorbed energy by ~30% and ~10% for the 10 and 100 nm spheres, respectively, over the whole range of impact distances as long as $b/r<1$. These differences correspond to restricted-LET values with cut-offs at Δ~350 eV and Δ~1.2 keV for the small and large site, respectively. (ii) Although a steep decrease is observed at about $b/r=1$, the explicit account of δ-ray transport in the MC simulations results in nonzero values for $b/r>1$. (iii) Differences between the vapor and liquid MC results are generally within the 10-15% level, whereas the phase effect in the LET calculations is only ~5%. The larger effect observed in the MC simulations is due to the additional phase effect on the transport of δ-rays. Nevertheless, in all cases, the mean event size for liquid is smaller because screening and polarization effects in the condensed phase reduce

the strength of particle-water interaction with a resulting increase of mean free paths. Thus, δ-ray escape from the site volume is more efficient in the liquid than in the vapor phase.

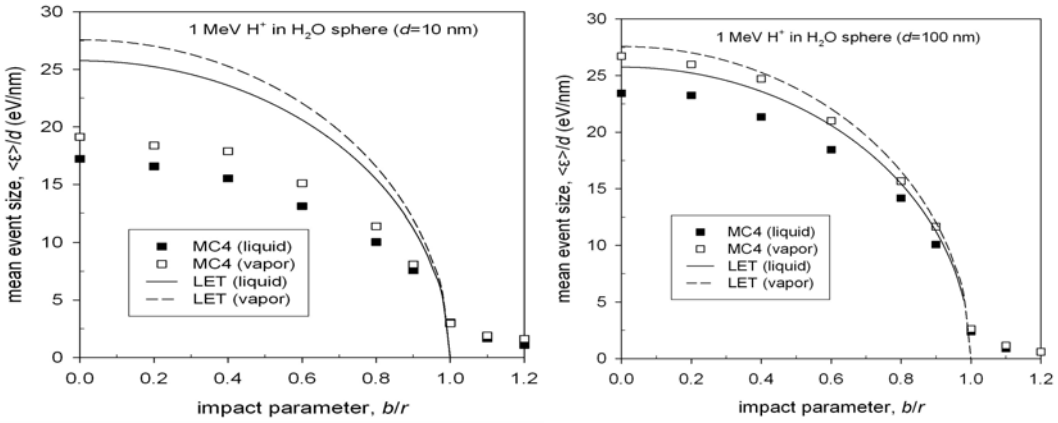

(a) (b)

Figure 5.1. The mean event size for 1 MeV protons as a function of the (normalized) impact distance for spheres having (a) 10 nm, and (b) 100 nm diameter. The lines are analytic calculations using the LET. Results on the two phases of water (both at unit density) are provided.

The δ-ray effect may be more clearly seen in Figure (5.2) where we present the ratio of the mean event size to LET for diametric traversals (b=0) as a function of the sphere diameter for 0.5, 1, and 5 MeV protons. The value of $\langle\varepsilon\rangle/d$ gradually approaches the LET with increasing site diameter and decreasing proton energy. The reason being that a larger site is capable of retaining more of the δ-rays generated within its volume, while the more energetic a proton is the less localized its track since $T_{\delta,max} \approx 4\ T_{proton}/1836$. The liquid curves are shifted to the right of the vapor ones due to the more diffused pattern of the track in the condensed phase. Evidently, for the typical proton energies examined here the failure of LET to

account for δ-ray effects leads to a significant overestimation (~10-60%) of energy deposition in sub-cellular volumes smaller than a few hundred nanometers. A similar trend for (<ε>/*d*)/LET has been obtained by MOCA [146]. Note that the straightforward solution to the above problem by the application of an energy- or spatially-restricted-LET to account for δ-ray efects, requires additional information with regard to (low energy) δ-ray transport and penetration which is not easily obtained either experimentally or theoretically.

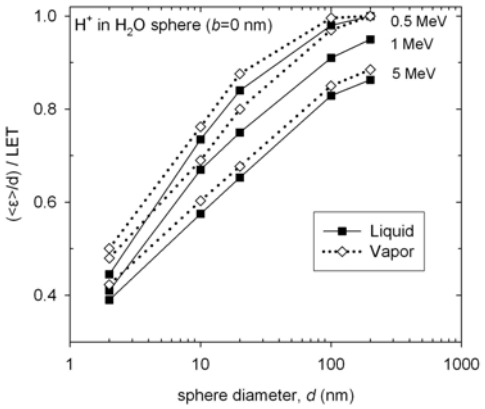

Figure 5.2. The ratio of the mean event size to the LET for 0.5, 1, and 5 MeV protons, as a function of the sphere diameter (the lines are to guide the eye). Results on the two phases of water (both at unit density) are provided.

Figure (5.3) presents event size straggling distributions for diametric traversals of 1 MeV protons in the two sites shown in Figure (5.1). The straggling of energy deposition depicted is a direct consequence of the statistical fluctuations in both the number of inelastic interactions experienced by the charged particles within the site and the amount of energy loss in each of these interactions. The influence of phase is noticeable—although not significant—in both panels. The less

spread-out pattern of the track in the vapor phase favors a larger fraction of δ-ray energy to be deposited near the proton track core which shifts the straggling distributions to the right. The shape of the distributions is approximately Gaussian for the 100 nm site where the mean and the most probable values are very close to each other. In contrast, strongly asymmetric, Poisson-like, shapes are obtained for the 10 nm site where the mean differs substantially from the most probable value.

Specifically, smaller energy deposition values are more probable than larger ones reflecting the properties of the single-collision spectrum. The transition from a Poisson-like to a Gaussian shape distribution is more clearly depicted in Figure (5.4) where we present event size straggling distributions for sites with a 2, 20, and 200 nm diameter. Although the results of Figure (5.4) pertain to the liquid phase, identical conclusions may be drawn from the vapor results. By virtue of the central

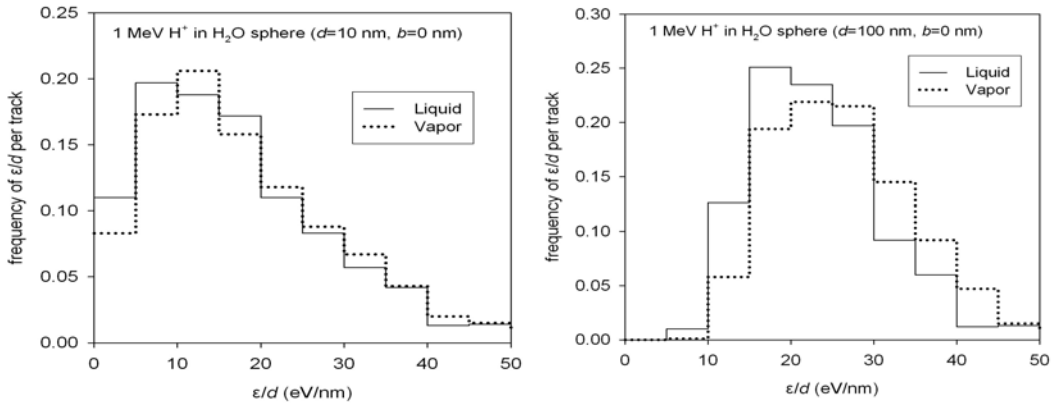

(a) (b)

Figure 5.3. Straggling distributions for 1 MeV protons crossing diametrically a sphere having (a) 10 nm, and (b) 100 nm diameter. Results on the two phases of water (both at unit density) are provided.

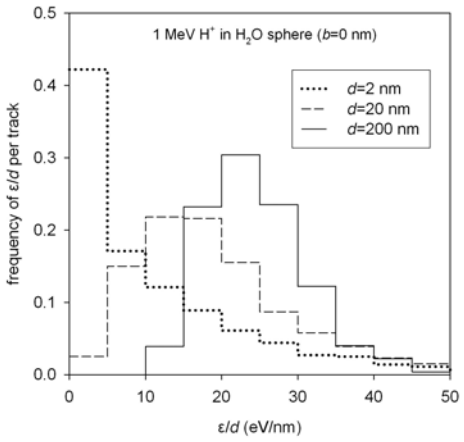

Figure 5.4. Straggling distributions for 1 MeV protons crossing diametrically spheres of various sizes (all calculations are for the liquid phase).

limit theorem, the higher the number of interactions that take place in a site the more symmetric the straggling distribution. Note that, whereas the mean event size calculated by the LET is ~26 eV/nm for all three sites depicted, the most probable event size decreases drastically as the site becomes smaller reaching 0-5 eV/nm for the 2 nm site. Although not shown, there is not any high tail in the presented straggling distributions similar to the one obtained for the conventional energy-loss straggling distributions [55]. The reason being that the straggling of energy imparted (as opposed to energy loss) is also influenced by the geometric boundaries of the site since, for not too large sites, hard energy-loss events do not contribute to the straggling of energy imparted because most of their energy is eventually deposited outside the volume through the energetic δ-rays. The importance of the straggling effect in connection to dosimetry is best revealed in Figure (5.5) where we present the ratio of the standard deviation to the mean absorbed energy in the

site. The relative error decreases with increasing site diameter and decreasing proton energy since it is generally inversely proportional to the (square root of the) number of inelastic interactions taken place within the site.

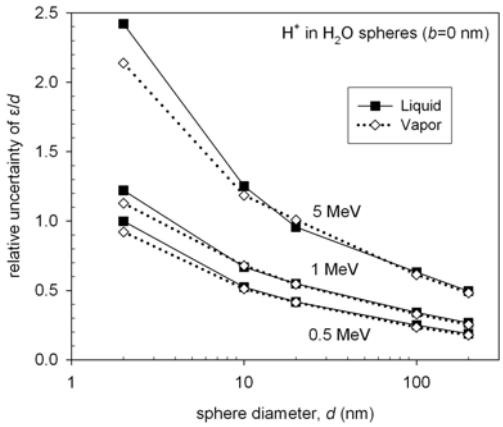

Figure 5.5. The relative error for the energy deposition (1 SD/mean) for protons of 0.5, 1, and 5 MeV crossing diametrically spheres of different sizes. Results on the two phases of water (both at unit density) are provided.

Clearly the concept of dose (and LET) may be entirely misleading for some combinations of proton energies and site diameters; for example, the relative error varies between ~20% for the largest site examined (200 nm) to much more than 100% for the smallest one (2 nm). An effect of similar magnitude has been observed for the LET of protons from energy-loss straggling distributions obtained by the OREC code [55]. The somewhat smaller relative error observed for the vapor phase (5-10%) is a consequence of the larger number of interactions in the site.

The above results may be extrapolated by simple arguments to other light ions in the range where the Bethe theory is valid. For example, additional

simulations with 2 to 20 MeV alpha particles confirmed that by virtue of the kinematics of knock-on collisions protons and alpha particles of the same velocity exhibit a similar δ-ray effect (<ε>/d vs. LET). Also, the relative error of alpha particles compared to protons scales inversely proportional to alphas (effective) charge (assuming +1 for protons). This is by virtue of the Poisson statistics that predicts a relative error proportional to the square root of the number of inelastic interactions within the site; the latter being proportional to the square of the projectile charge.

5.4 Conclusion

The effect of δ-rays and straggling is shown to be of significant importance to proton and alpha-particle dosimetry of sub-cellular volumes ranging from few to few hundred nanometers. This is the spatial scale of DNA and chromatin structures which are known to be critical targets for radiation induced biological effects. It is shown that LET-based calculations may be in error by a significant margin while the stochastic fluctuations may render the very concept of dose entirely misleading. The effect of phase (vapor vs. liquid at the same density), although of smaller magnitude than the above effects, has a noticeable impact on the results. The present work contributes to a more accurate prediction of various dosimetric and stochastic quantities at the sub-cellular scale where simple analytic calculations are invalid. In the long-term it is expected that the implementation of such results into

biophysical models of radiation effects will result in more realistic predictions on the efficacy of radiotherapeutic modalities that employ either external proton beam irradiation or internal alpha-emitting radionuclides.

Chapter 6

Concluding remarks

6.1 Summary

In Chapter 2 we were interested in the transport and energy loss of low-energy electrons in water in the liquid phase. The inelastic model for energy loss was based on a semi-empirical dielectric-response function for the valence-shells of the liquid whereas an exchange corrected semi-classical formula was used for K-shell ionization. We parameterized the dielectric cross-sections of the liquid in accordance with the Bethe asymptote, thus providing a unified approach for both phases of water and greatly facilitating the computations. Born corrections at lower energies were implemented. Angular deflections were determined by empirical schemes established from vapor data. Electron tracks generated by the code were used to calculate energy- and interaction-point-kernel distributions at low electron energies in liquid water. The effect of various model assumptions (e.g. dispersion,

Born-corrections, phase) on both the single-collision and slowing-down distributions was examined.

In Chapter 3 we extend our analysis to water in vapor. We compare results for water in vapor and liquid phase at the same density. A unified methodology for both phases has been implemented in the Monte-Carlo code based on elements of the Born and Bethe theories which are used to establish cross-sections for inelastic electronic scattering, the main mechanism of energy loss in the presented study. The linear dielectric response theory was used for the valence shells of the liquid phase implemented by Born-corrections at low energies. Monte-Carlo calculations of the spatial pattern of energy distribution, as well as the clustering properties of collision events in full slowing-down electron tracks have been performed for both the vapor and liquid phases. The degree in which various model assumptions pertaining to the condensed-phase influence the above distributions was examined.

In Chapter 4 we focus our attention to the transport of energetic non-relativistic protons in both the vapor and liquid phases of water. A unified particle-water inelastic model for both phases of water has been developed based on experimental optical data and elements of the Bethe theory. The model applies to both electrons and heavy charged particles. Condensed-phase effects are included in the liquid version (MC4L) by means of the dielectric functions which, essentially, substitute the oscillator-strength used in the vapor version (MC4V). Results in the form of radial dose distributions and spatially-restricted LET are presented and compared with the literature.

In Chapter 5 our detailed-history Monte-Carlo code (MC4) was used to study the energy deposition from proton and alpha particle tracks at the sub-cellular level. Inelastic cross sections for both the vapor and liquid phases of water have been implemented into our code in order to explore the influence of non-linear density effects associated with the condensed-phase cellular environment. We present results of energy deposition and its straggling for 0.5 to 5 MeV/amu protons and alpha particles traversing or passing near spherical volumes of 2 to 200 nm in diameter relevant to DNA- and chromosome-size targets. Protons and alpha particles of the same velocity exhibit a δ-ray effect whereas the relative error of the alphas is almost half that of protons. The effect of phase is noticeable (10-15%) mainly through differences on the transport of δ-rays which in liquid water have higher penetration distances.

6.2 Future directions

Since the formulae used for the inelastic cross sections rely mostly on particle-theoretic approach, it is expected that our simulation code can be of value in a wider variety of circumstances, where experimental results are not yet available.

The most obvious example is to adjust the Monte-Carlo code to simulate particle transport in a non-uniform medium or in two or more media. This has limitless applications, e.g. transport in a living cell's core, focusing on the cell's

DNA, submerged in a liquid medium. This will lead to a better approximation to the DNA damage problem and to other multi-scale biophysical models. Better understanding and quantifying of such radiation effects will result to a more realistic prediction on the effectiveness of new radio therapeutic modalities that employ either external proton beam irradiation or internal alpha-emitting radionuclides.

As a final note, the analysis presented here is only for the *physical stage* of the process. Each track takes real time of the order of a fento-sec ($=10^{-15}$ seconds), and when it ends, along with water molecules we are left with some ions and secondary electrons that were generated by ionization of the medium's atoms or molecules. What follows next is the *chemical stage* and then the *biological stage*. The analysis of the chemical stage is a subject of *radiochemistry*, whereas the biological stage is a subject of *biochemistry*. Ultimately we will be able to see how controlled incident radiation can enhance or obstruct a cell's biological processes, with obvious advances in the therapeutic area, the treatment of cancer and other cell-related diseases.

Chapter 7

Outline of the code

7.1 Explicit assumptions

Some of the basic assumptions have already been noted, but are listed here for clarity, in more detail:

The trajectory of a particle consists of a collection of straight-line segments connecting consecutive interaction events. This is the case when the incident radiation wavelength is small compared to the inter-atomic distances, leading to incoherent scattering (see Chapter 1).

Protons do not experience any angular deflection; this is the “straight-path approximation”. This is justified for the energies considered since protons are approximately 1837 times heavier than electrons.

Excitation events induce no angular deflection.

All collisions have cylindrical symmetry. In local polar coordinates (r, θ, φ) where the incoming particle direction corresponds to the polar axis, this reduces to φ~U[0,2π). Equivalently all collisions are assumed *head-on*.

Photons produced by impact excitation and impact ionization as well as particles with energy below the chosen cutoff value are assumed to deposit their energy instantaneously "at the spot", that is at the point of their production (see Section (1.2))

As energy cutoff value we use $E_{\min} = 7.4\,eV$ which is the minimum excitation potential for water molecules. This assumption is necessary since a particle with KE less than $E_{\min}$ experiences only elastic scattering. Without such a constraint the stack of particles eventually fills up with secondary electrons with small energies and the code might run indefinitely.

All collisions are assumed non-relativistic. This is justified noting that $E \ll mc^2$ where E and m are projectile K.E. and mass for all runs. It is of consequence that the magnetic field can be ignored and all interaction happens under a coulomb electrostatic field.

7.2 The algorithm

The main loop of the algorithm used is shown in Algorithm 1 (Figure (7.1)). It simulates transport of one projectile, and is repeated until we get an accurate

distribution of the quantities of interest. At each stage of the program we have a stack of particles of energy greater than the cutoff. At the start the stack consists of one particle, the primary, with given energy and direction of motion, as is customary, on the z-axis . The term "particle data" refers to particle type, position, direction of motion and energy. The term "collision data" refers to interaction occured, energy deposited and (excitation or ionization) orbital. The term "DETERMINE:" implies that the quantities of interest are obtained by sampling the (discrete or continuous) relevant probability distribution defined by the corresponding cross section, using computer-generated random numbers (see Algorithms 2,3,4 in Figures (7.2)-(7.4)).

Algorithm 2 (Figure(7.2)) is used to determine the distance to next interaction (event-to-event distance), X. It is easy to show that X follows the exponential distribution with parameter σ_{total} given by equation (1.7), according to equation (1.6). After computing the DNI, the next collision point is calculated, given the position and direction of current particle.

The next step is to determine what type of interaction will take place there. This is done by sampling from a discrete distribution, using Algorithm 3 (Figure (7.3)), with $n = 3, \sigma_1 = \sigma_{elastic}, \sigma_2 = \sigma_{excitation}, \sigma_3 = \sigma_{ionization}$. Note that σ_{total} is given by equation (1.7) as the sum of $\sigma_{elastic}$, $\sigma_{excitation}$ and $\sigma_{ionization}$. The resulting type of interaction follows the distribution given in (1.8).

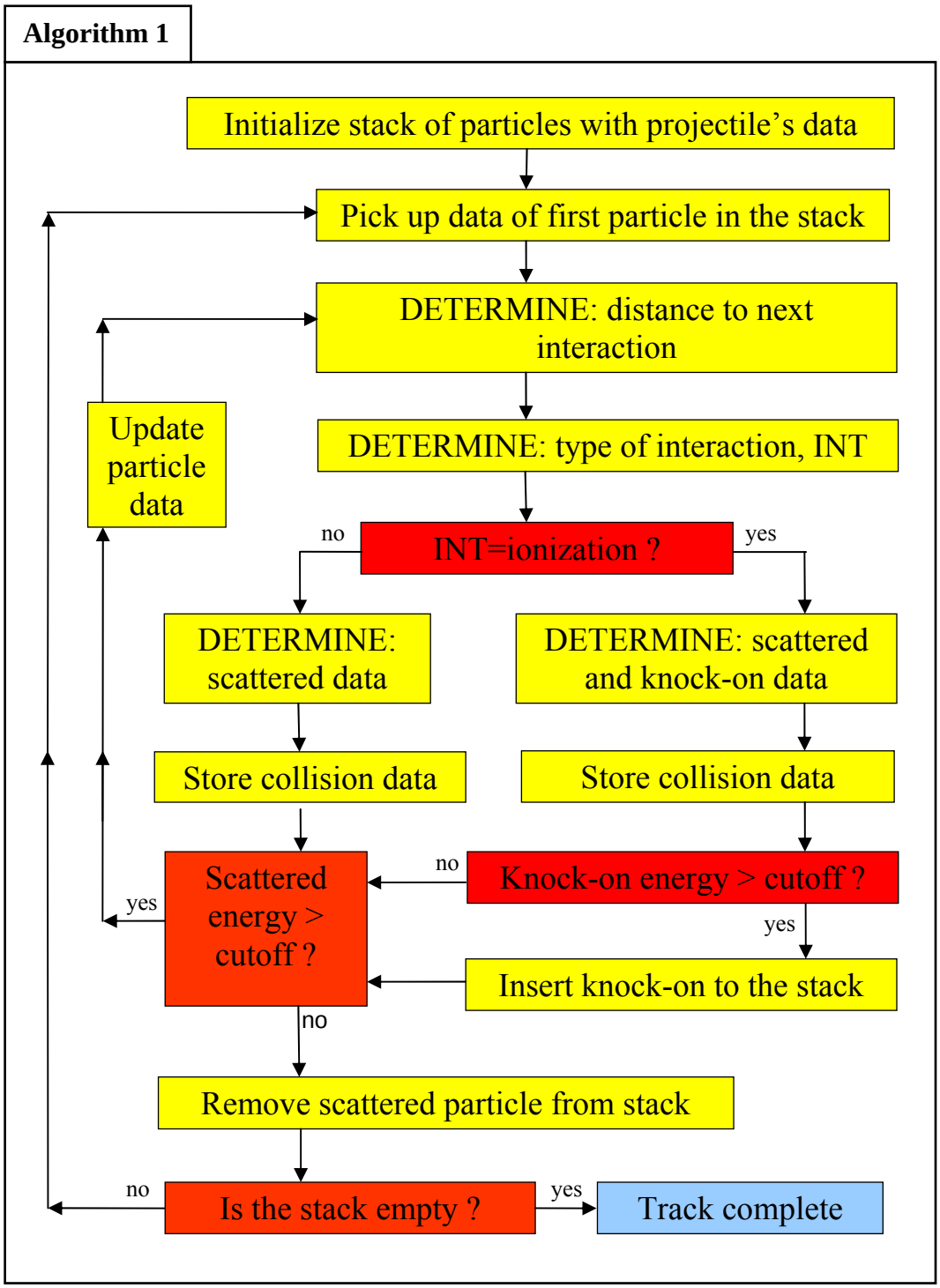

Figure 7.1 The main loop that runs transport of one projectile and stores collision data.

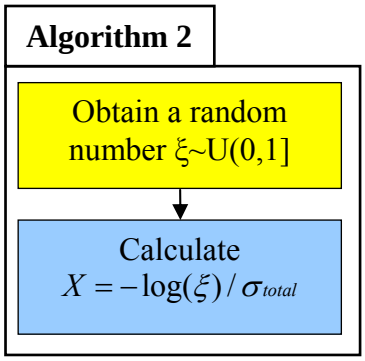

Figure 7.2. Determining the distance to next interaction, *X*.

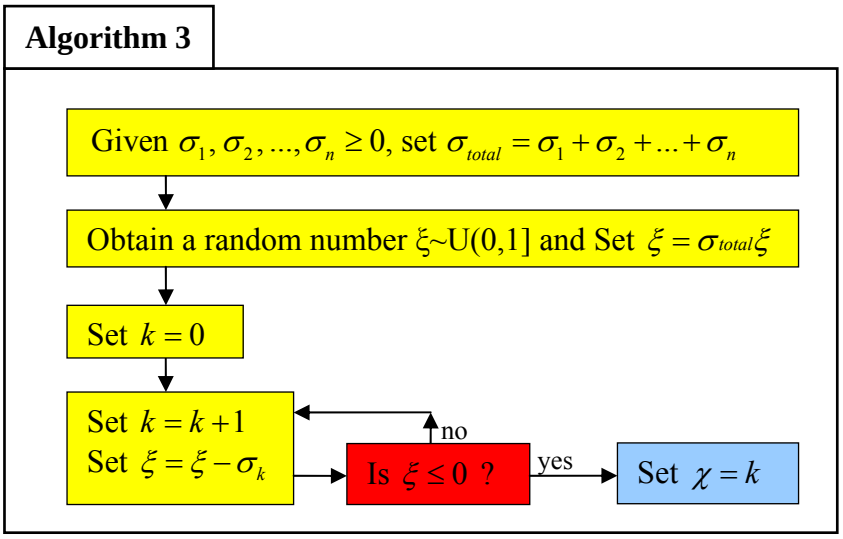

Figure 7.3. Sampling from a discrete distribution. Used to determine type of interaction and orbital of inelastic collisions.

Finally we need an algorithm that will determine particle data, following an event, of given continuous spectrum. There is no analytic solution to this since the

cross-sections formulae are complicated. To this end we use the computational *rejection sampling method*, which is depicted on Algorithm 4 (Figure (7.4)). The distribution of the output χ is $f(\chi)=\frac{d\sigma}{d\chi}$. Here χ can be energy or scattering angle of scattered or knock-on (in ionization) particle. The support of $f(\chi)$ is the interval $[\chi_{\min},\chi_{\max}]$ and the value $f_{\max}=\max\{f(\chi),\chi\in[\chi_{\min},\chi_{\max}]\}$. The rejection sampling method pictorially is shown in Figure (7.5).

After we determine energy and scattering angles of outgoing particles following an inelastic collision the corresponding orbital is selected by sampling from a discrete distribution, using Agorithm 3 (Figure (7.3)).

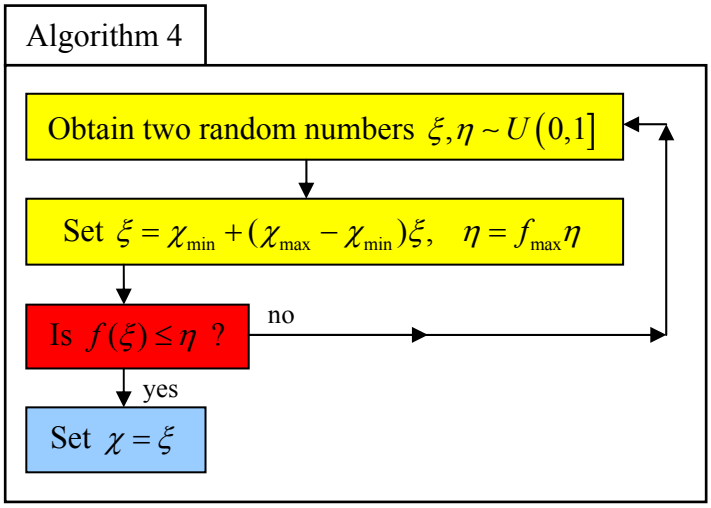

Figure 7.4. Rejection sampling method: sampling from a continous distribution. Used to determine outgoing particle data: Scattered particle for elastic collisions and excitations, scattered and knock-on particles for ionizations.

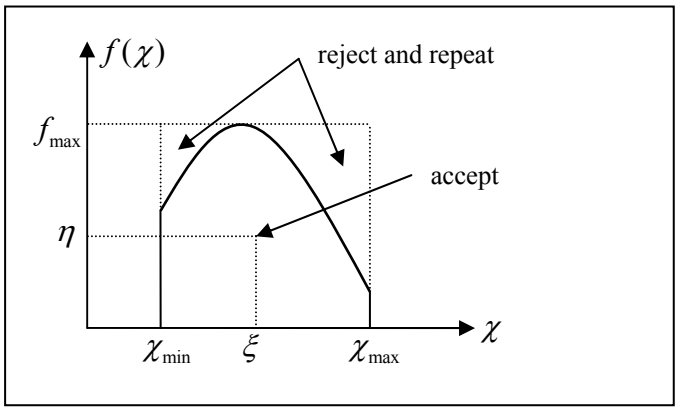

Figure 7.5. Illustration of the rejection sampling method.

Rejection sampling method is a sequence of rejected trials followed by an accepted one. Each trial consists of a point uniformly distributed inside the plane box $[\chi_{\min}, \chi_{\max}] \times [0, f_{\max}]$. A trial (ξ, η) is accepted if $f(\xi) \le \eta$ and rejected otherwise. Note that it is not necessary to find *exactly* the value of $f_{\max}$, since this is often a long and tedious procedure. Using any upper bound of f will produce numbers of the same distribution. However, increasing $f_{\max}$ too much increases the probability of rejection and the expected number of rejected trials, which is computer-time consuming.

7.3 Computing random numbers

When we refer to computer-generated random numbers it is assumed that a deterministic pseudo-random routine is used. Most programming languages have a built-in pseudo-random number routine which returns numbers that resemble random numbers uniformly distributed in the interval (0,1]. Given the finite numerical precision of the machine, it is a map from a finite set onto itself. Therefore, all such routines produce a sequence of numbers that repeats itself after a given number of evaluations. The one used initially in the simulation produced a periodic sequence of numbers with period 2^{24}=16,777,216 evaluations. So each time we run the simulation (with all other input parameters being equal) we get the same results.

This problem is overcome by selecting an initial seed for the random number routine that depends on the current date and time, thus generating different numbers in every call. This is called *randomizing* and can be invoked at the beginning and at any point of program execution. When the code starts we are given the option of selecting the same set of random numbers or a different set by randomizing. Choosing to use the same random numbers will produce the same output every time. This is useful in the debugging stage of the code: once some error or unexpected behavior occurs at some point of execution we can repeat the exact calculation to see what went wrong and correct it. In the running stage where all errors and bugs have been cleared, we only use randomizing.

Bibliography

[1] Akkerman A, Akkerman E, 1999, Characteristics of electron inelastic interactions in organic compounds and water over the energy range 20-1000 eV, *J. Appl. Phys.* **86,** 5809-5816.

[2] Akkerman A, Barak J, 2002, Ion-track structure and its effects in small size volumes of silicon IEEE Trans. *Nucl. Sci.* **49**, 3022-3031.

[3] Ashley J C, 1991, Energy-loss probabilities for electrons, positrons, and protons in condensed matter, *J. Appl. Phys.* **69,** 674-678.

[4] Ashley J C, 1991, Optical-data model for the stopping power of condensed matter for protons and antiprotons, *J. Phys. Condens. Matter* **3,** 2741-2753.

[5] Ballarini F, Biaggi M, Merzagora M, Ottolenghi A, Dingfelder M, Friedland W, Jacob P, Paretzke HG, 2000, Stochastic aspects and uncertainties in the prechemical and chemical stages of electron tracks in liquid water: a quantitative analysis based on Monte-Carlo simulations. *Radiat. Environ. Biophys.* **39,** 179-188.

[6] Banna M S, McQuaide B H, Malutzki R, Schmidt V, 1986, *J. Chem. Phys*. **84,** 4739.

[7] Baro J, Sempau J, Fernandez-Varea J M, Salvat F, 1995, PENELOPE: an algorithm for Monte-Carlo simulation of the penetration and energy loss of electrons and positrons in matter, *Nucl. Instr. Meth.* B, **100,** 31-46.

[8] Beenakker C I M, De Heer F J, Krop H B, Mohlmann G R, 1974, *Chem. Phys*. **6,** 445.

[9] Berger M J, 1963, *Methods in Computational Physic* (New York : Academic), **1,** 135.

[10] Berger M J, 1985, *Radiat. Prot. Dosim*. **13,** 87.

[11] Berger M J, 1988, *Phys. Med. Biol*. **33,** 583.

[12] Bethe H, 1953, *Phys. Rev*. **89,** 1256.

[13] Bichsel H, 1993, *J. Chim. Phys*. **90,** 617.

[14] Bichsel H, 1998, *Rev. Mod. Phys*. **60,** 663.

[15] Bigildeev E A, Michalik V, 1996, Charged particle tracks in water of different phases. Monte-Carlo simulation of electron tracks, *Radiat. Phys. Chem*. **47,** 197-207.

[16] Bolorizadeh M A, Rudd M E, 1986, *Phys. Rev*. A **33,** 882.

[17] Brenner D J, Zaider M, 1983, A computationally convenient parameterization of experimental angular distributions of low energy electrons elastically scattered off water vapour *Phys. Med. Biol*. **29,** 43-447.

[18] Brion C E, Carnovale F, 1985, *Chem. Phys*. **100,** 291.

[19] Brion C E, Thomson J P, 1984, *J. Electron Spectr. Rel. Phenom*. **33,** 301.

[20] Chen J, Kellerer A M, 1997, Calculation of radial dose distributions for heavy ions by a new analytic approach. *Radiat. Prot. Dosim*. **70**, 55-58.

[21] Chen J, Kellerer A M, Rossi H H, 1994, Radially restricted linear energy transfer for high-energy protons: a new analytic approach. *Radiat. Environ. Biophys*. **33**, 181-187.

[22] Cobut V, Frongillo Y, Patau J P, Goulet T, Fraser M J, Jay-Gerin J P, 1998, Monte-Carlo simulation of fast electron and proton tracks in liquid water: I. Physical and physicochemical aspects, *Radiat. Phys. Chem*. **51,** 229-243.

[23] Cucinotta F A, Nikjoo H, Goodhead D T, 1999, Applications of amorphous track models in radiation biology. *Radiat. Environ. Biophys*. **38**, 81-92.

[24] Dingfelder M, Friedland W, 2001, Basic data for track structure simulations: electron interaction cross-sections in liquid water, *Advanced Monte-Carlo for Radiation Physics, Particle Transport Simulation and Applications* (Berlin: Springer), 267-272.

[25] Dingfelder M, Inokuti M, 1999, The Bethe surface of liquid water Radiat. *Environ. Biophys*. **38,** 93-96.

[26] Dingfelder M, Hantke D, Inokuti M, Paretzke H G, 1998, Electron inelastic-scattering cross sections in liquid water, *Radiat. Phys. Chem*. **53,** 1-18.

[27] Dingfelder M, Inokuti M, Paretzke H G, 2000, Inelastic-collision cross sections of liquid water for interactions of energetic protons. *Radiat. Phys. Chem*. **59**, 255-275.

[28] Djuric N Lj, Cadez I M, Kurepa M V, 1988, Int. *J. Mass Spectrom. Ion Proc*. **83,** R7.

[29] Emfietzoglou D, 1996, *PhD Thesis*, Georgetown University, Washington, DC.

[30] Emfietzoglou D, 2001, Inelastic cross-sections for use in Monte-Carlo track structure codes, *Advanced Monte-Carlo for Radiation Physics, Particle Transport Simulation and Applications*, (Berlin: Springer), 273-278.

[31] Emfietzoglou D, 2002, Semi-empirical inelastic cross-sections for electron transport in liquid water, *Radiat. Prot. Dosim*. **99,** 39-46.

[32] Emfietzoglou D, 2003, Inelastic cross-section for electron transport in liquid water: a comparison of dielectric models *Radiat. Phys. Chem*. **66,** 373-385.

[33] Emfietzoglou D, Moscovitch M, 2002 M Inelastic collision characteristics of electrons in liquid water, *Nucl. Instr. Meth*. B **193,** 71-78.

[34] Emfietzoglou D, Moscovitch M, 1999, *Phys. Med. Biol*. **44,** 207.

[35] Emfietzoglou D, Papamihael G, Kostarelos K, Moscovitch M, 2000a, A Monte-Carlo track structure code for electrons (10 eV-10 keV) and protons (0.3-10 MeV) in water: partitioning of energy and collision events *Phys. Med. Biol*. **45,** 3171-3194.

[36] Emfietzoglou D, Papamihael G, Moscovitch M, 2000b, An event-by-event computer simulation of interactions of energetic charged particles and all their secondary electrons in water, *J. Phys. D: Appl. Phys*. **33,** 932-944.

[37] Emfietzoglou D, Moscovitch M, Pathak A, 2003, *Nucl. Instr. and Meth*. B **212,** 101.

[38] Emfietzoglou D, Moscovitch M, 2002, *Nucl. Instr. and Meth*. B **193,** 71-78.

[39] Emfietzoglou D, Papamichael G, Moscovitch M, 2000, *J. Phys. D* **33,** 932.

[40] Emfietzoglou D, Cucinotta F, Nikjoo H A, 2005, complete dielectric response model for liquid water: a solution of the Bethe ridge problem. *Radiat. Res*. **164**, 202-211.

[41] Emfietzoglou D, Moscovitch M, 2003, Secondary electron spectra for fast proton impact on gaseous and liquid water, *Nucl. Instrum. Methods* **B209**, 239-245.

[42] Emfietzoglou D, Nikjoo H, 2005, The effect of model approximations on single-collision distributions of low-energy electrons in liquid water. *Radiat. Res***. 163**, 98-111.

[43] Evans T M, Wang C K C, 1999, *Radiat. Res.* **151,** 19.

[44] Fernandez-Varea J M, Liljequist D, Csillag S, Raty R, Salvat F, 1996, Monte-Carlo simulation of 0.1-100 keV electron and positron transport in solids using optical data and partial wave cross sections, *Nucl. Instr. Meth*. B **108,** 35-50.

[45] Friedland W, Bernhardt P, Jacob P, Paretzke HG, Dingfelder M, 2002, Simulation of DNA damage after proton and low LET irradiation, *Radiat. Prot. Dos*. **99,** 99-102.

[46] Goodhead D T, 1985, Relationship of microdosimetric techniques to applications in biological systems, *The Dosimetry of Ionizing Radiation*, **2** (Orlando, FL: Academic), 1-89.

[47] Goodhead D T, 1994, Initial events in the cellular effects of ionizing radiation: clustered damage in DNA, *Int. J. Radiat. Biol*. **65,** 7-17.

[48] Goodhead D T, 1995, *The Dosimetry of Ionizing Radiation*, **2** (Orlando, FL: Academic), 1.

[49] Goodhead D T, 1989, The initial physical damage produced by ionizing radiations. *Int. J. Radiat. Biol*. **56**, 623-634.

[50] Green A E S, Stolarski R S, 1972, Analytic models of electron impact excitation cross sections, *J. Atmos. Terr. Phys*. **34,** 1703-1717.

[51] Grosswendt B, Waibel E, 1978, Transport of low energy electrons in nitrogen and air, *Nucl. Instrum. Meth*. **155,** 145-156.

[52] Grosswendt B, and Baek W Y W, 1998, values and radial dose distributions for protons in TE-gas and air at energies up to 500 MeV. *Phys. Med. Biol*. **43**, 325-337.

[53] Grosswendt B, 2005, Nanodosimetry, from radiation physics to radiation biology. *Radiat. Prot. Dosim*. **115**, 1-9.

[54] Hamm R N, Wright H A, Ritchie R H, Turner J E, Turner T P, 1975, Monte-Carlo transport of electrons through liquid water, *5th Symposium on Microdosimetry* (Brussels: EUR-5452 EC), 1037-1050.

[55] Hamm R N, Turner J E, Wright H A, 1985, Statistical fluctuations in heavy charged particle tracks. *Radiat. Prot. Dosim*. **13**, 83-86.

[56] Hamm R N, Wright H A, Richie R H, Turner G E, Turner T P, 1975, MonteCarlo transport of electrons through liquid water *5th Symp. Microdosimetry* (Brussels) EUR-5422EC, 1037-1050.

[57] Hayashi H, Watanabe N, Udagawa Y, Kao C C, 2000, The complete optical spectrum of liquid water measured by inelastic x-ray scattering, *Proc. Natl. Acad. Sci*. **97,** 6264-6266.

[58] Heller J M, Hamm R N, Birkhoff R D, Painter L R, 1974, Collective oscillatio in liquid water, *J. Chem. Phys*. **60,** 3483-3486.

[59] Hill M A, Smith F A, 1994, Calculation of initial and primary yields in the radiolysis of water, *Int. J.Appl. Radiat. Isot. Phys. Chem*. **43,** 265-280.

[60] Hippler R, 1990, Plane wave Born calculations of K-shell ionization at low velocities, *Phys. Letters A* **144,** 81-85.

[61] Horowitz Y S, 1981, *Phys. Med. Biol*. **26,** 765.

[62] Hubbard J, 1955, The dielectric theory of electronic interactions in solids, *Proc. Phys. Soc*. (London) **A68,** 976-986.

[63] IAEA, 1995, Atomic and molecular data for radiation therapy and related research, *IAEA-TECDOC-799,* (Vienna: IAEA).

[64] ICRU, 1983, Microdosimetry, *ICRU Report* **36,** (Bethesda, MD: ICRU)

[65] ICRU, 1986, The quality factor in radiation protection *ICRU Report* **40,** (Bethesda, MD: ICRU)

[66] ICRU, 1993, Stopping powers and ranges for protons and alpha particles, *ICRU Report* **49,** (Bethesda, MD: ICRU)

[67] ICRU, 1996, Secondary electron spectra from charged particle interactions, *ICRU Report* **55,** (Bethesda, MD: ICRU)

[68] Inokuti M, 1971, Inelastic collisions of fast charged particles with atoms and molecules – The Bethe theory revisited, *Rev. Mod. Phys*. **43,** 297-347.

[69] Inokuti M, 1991, Radiat. Eff. Defects Solids **117,** 143 943.

[70] Interactions and Energy Transport in the Condensed Phase, 1991, *Physical and Chemical Mechanisms in Molecular Radiation Biology* (New York: Plenum Press), 99.

[71] Ito A, 1988, Electron track simulation for microdosimetry Monte-Carlo Transport of Electrons and Photons (*New York: Plenum*), 361-382.

[72] Jackson J D, McCarthy R L, 1972, z3 corrections to energy loss and range, *Phys. Rev. B* **6,** 4131-4141.

[73] Jain D K, Khare S P, 1976, *J. Phys. B: At. Mol. Phys*. **9,** 1429.

[74] Kaushik Y D, Khare S P, Kumar A, 1981, *Physica C* **106,** 135.

[75] Kellerer A M, 1985, Fundamentals of microdosimetry. In: *The Dosimetry of Ionizing Radiation* (New York: Academic Press), 77-162.

[76] Kim Y K, 1975, Energy distribution of secondary electrons, *Radiat. Res.* **64,** 96-105.

[77] Kim Y K, 1975, Energy distribution of secondary electrons I. Consistency of experimental data, *Radiat. Res.* **61,** 21-35.

[78] Kutcher G J, Green A E S, 1976, A model for energy deposition in liquid water, *Radiat. Res.* **67,** 408.

[79] Landau L, Lifshitz E M, 1965, *Quantum Mechanics. Nonrelativistic Theory* (London: Pergamon).

[80] Lappa A V, Bigildeev E A, Burmistov D S, Vasilyev O N, 1993, «Trion» code for radiation action calculatios and its application in microdosimetry and radiobiology, *Radiat. Environ. Biophys*. **32,** 1.

[81] LaVerne J A, Mozumder A, 1993, Conceming plasmons excitation in liquid water, *Radiat. Res.* **133,** 282-288.

[82] Lindhard J, 1954, On the properties of a gas of charged particles, *Kgl. Dan. Vidensk. Mat. Fys. Medd*. **28,** 1-57.

[83] Lund J C, Sinclair F, Entine G, 1986, *IEEE Trans. Nucl .Sci*. **33,** 620.

[84] Mayol R, Salvat F, 1990, Cross sections for K-shell ionization by electron impact, *J. Phys. B: At. Mol. Opt. Phys.* **23,** 2117-2130.

[85] Michalik V, 1992, Model of DNA damage induced by radiations of various qualities, *Int. J. Radiat. Biol*. **62,** 9-20.

[86] Miller J H, 1989, Prediction of secondary electron energy spectra, *Nucl. Tracks Radiat. Meas*. **16,** 207-211.

[87] Miller J H, Wilson W E, Manson S T, 1985, Secondary electron spectra: a semiempirical model, *Radiat. Prot. Dosim*. **13,** 27-30.

[88] Miller J H, Wilson W E, Manson S T, Rudd M E, 1987, Differential cross sections for ionization of water vapor by high velocity bar, *J. Chem. Phys*. **86,** 157.

[89] Miller W F, Platzman R L,1957, *Proc. Phys. Soc*. **A 70,** 299.

[90] Mohlmann G R, De Heer F J, 1979, *Chem. Phys*. **40,** 157.

[91] Moliere G, 1947, *Z. Naturf. a* **2,** 133.

[92] Moliere G, 1948, *Z. Naturf. a* **3,** 78.

[93] Moscovitch M, Emfietzoglou D, 1997, *J. Appl. Phys*. **81,** 58.

[94] Moscovitch M, Horowitz Y S, 1988, *J. Phys. D: Appl. Phys*. **21,** 804.

[95] Nahum A E, 1999, Condensed-history Monte-Carlo simulation for charged particles *Radiat. Environ. Biophys*. **38**, 163-173.

[96] Nikjoo H, Goodhead D T, 1991, Track structure analysis illustrating the prominent role of low-energy electrons in radiobiological effects of low-LET radiations, *Phys. Med. Biol*. **36,** 229-238.

[97] Nikjoo H, O'Neill P, Wilson W E, Goodhead D T, 2001, Computational approaches for determining the spectrum of DNA damage induced by ionizing radiation, *Radiat. Res*. **156,** 577-583.

[98] Nikjoo H, O'Neill P, Terrisol M, Goodhead D T, 1994, Modeling of radiation-induced DNA damage: the early physical and chemical event, *Int. J. Radiat. Biol*. **66,** 453-457.

[99] Nikjoo H, Terrisol M, Hamm R N, Turner J E, Uehara S, Paretzke H G, Goodhead D T, 1994, Comparison of energy deposition in small cylindrical volumes by electrons generated by Monte-Carlo track structure codes for gaseous and liquid water, *Radiat. Prot. Dosim*. **52,** 165-169.

[100] Nikjoo H, Uehara S, Brenner D J, 1997, Microdosimetry: An Interdisciplinary Approach eds D T Goodhead et al (*Cambridge: The Royal Society of Chemistry*),3.

[101] Nikjoo H, Uehara S, Wilson W E, Hoshi M, Goodhead D T, 1998, *Int. J. Radiat. Biol*. **73,** 355-364.

[102] Nikjoo H, Uehara S, 1994, Computational approaches in molecular radiation biology, *Plenum Press*, New York, 167.

[103] Nikjoo H, Khvostunov I K, Cucinotta F, 2002, The response of tissue-equivalent proportional counters to heavy ions, *Radiat. Res*. **157**, 435-445.

[104] Nikjoo, H., Uehara, S., Emfietzoglou, D., Cucinotta F, 2006, A Monte-Carlo Track Structure Codes in Radiation Research – A Review. *Radiat. Meas*. **41,** 1052–1074.

[105] NIST, 1984, Physical Reference Data Stopping-power and range tables for electrons web page http://www.physics.nist.gov/ 944.

[106] Olivero J, Stagat R W, Green A E S, 1972, *J. Geophys. Res*. **77,** 4797.

[107] Opal C B, Beaty E C, Peterson W K, 1972, Tables of secondary-electron-production cross-sections, *At. Data* **4**, 209-253.

[108] Ottolenghi A, Ballarini F, Merzagora M, 1999, Modeling radiation-induced biological lesions: from initial energy depositions to chromosome aberrations. *Radiat. Environ. Biophys*. **38**, 1-13.

[109] Paretzke H G, 1987, Radiation track structure theory, *Kinetics of Non-homogeneous Processes,* ed G R Freeman (*New York: Wiley*), 89-170.

[110] Paretzke H G, Turner J E, Hamm R N, Ritchie R H, Wright H A, 1991, *Radiat. Res*. **127,** 121.

[111] Paretzke H G, Turner J E, Hamm R N, Wright H A, Ritchie R H, 1986, Calculated yields and fluctuations for electron degradation in liquid water and water vapor, *J. Chem. Phys*. **84,** 3182-3188.

[112] Pimblott S M, Mozumder A, 1991, J. *Phys. Chem***. 95,** 7291.

[113] Pimblott S M, LaVerne J A, Mozumder A, Green N J B, 1990, Structure of electron tracks in water. 1. Distribution of energy deposition events, *J. Phys. Chem*. **94,** 488-495.

[114] Raeside D E, 1976, *Phys. Med. Biol*. **21,** 181.

[115] Ritchie R H, 1959, Interaction of charged particles with a degenarate Fermi-Dirac electron gas, *Phys. Rev*. **114,** 644-654.

[116] Ritchie R H, Howie A, 1977, Electron excitation and the optical potential in electron microscopy, *Philos. Magazine* **36,** 463-481.

[117] Ritchie R H, Hamm R N, Turner J E, Wright H A, 1978, The interaction of swift electrons with liquid water, *Proc. 6th Symp. on Microdosimetry* (Luxemburgh: Harwood Academic), 345-354.

[118] Ritchie R H, Hamm R N, Turner J E, Wright H A, Ashley J C, 1989, *Nucl. Tracks Radiat. Meas*. **16,** 141.

[119] Ritchie R H, Hamm R N, Turner J E, Wright H A, Bloch W E, 1991, Radiation interactions and energy transport in the condensed phase, *Physical and Chemical Mechanisms in Molecular Radiation Biology* (New York: Plenum), 99-136.

[120] Rogers D W O, Bielajaw A F, 1990, *The Dosimetry of Ionizing Radiation*, vol **3** (Orlando, FL: Academic), 427.

[121] Rossi H, Zaider M, 1996, Microdosimetry and its Applications (*Berlin: Springer*).

[122] Rudd M E, Goffe T V, DuBois R D, Toburen L H, 1985, *Phys. Rev***. A 31,** 492.

[123] Rudd M E, Kim Y-K, Madison D H, Gay T J, 1992, *Rev.Mod. Phys*. **64,** 441.

[124] Salvat F, Fernandez-Varea J M, 1992, Semiempirical cross sections for the simulation of the energy loss of electrons and positrons in matter, *Nucl. Instr.Meth*. **B63,** 255-269.

[125] Salvat F, Martinez J D, Mayol R, Parellada J, 1985, *J. Phys. D* **18,** 299-315.

[126] Schutten J, De Heer F J, Moustafa H R, Boerboom A J H, Kistemaker J, 1966, *J. Chem. Phys*. **44,** 3924.

[127] Senger B, Falk S, Rechenmann R V, 1990, *Radiat. Prot. Dosim*. **31,** 37.

[128] Terrisol M, Beaudre A, 1990, Simulation of space and time evolution of radiolytic species induced by electrons in water, *Radiat. Prot. Dosim*. **31,** 171-175.

[129] Toburen L H, Wilson W E, 1977, *J. Chem. Phys*. **66,** 5202.

[130] Toburen L H, Wilson W E, Popowich R J, 1980, *Radiat Res*. **82,** 27.

[131] Tung C J, Chen Y F, Kwei C M, Chou T L, 1994, Differential cross sections for plasmon excitations and reflected electron-energy-loss spectra, *Phys. Rev*. **B49**, 16684-16693.

[132] Turner J E, Hamm R N, Wright H A, Ritchie R H, Magee J L, Chatterjee A, Bolch W E, 1988, *Radiat. Phys. Chem***. 32,** 503.

[133] Turner J E, Paretzke H G, Hamm R N, Wright H A, Ritchie R H, 1982, Comparatice study of electron energy deposition and yields in water in the liquid and vapor phases, *Radiat. Res*. **92,** 47-60.

[134] Uehara S, Nikjoo H, Goodhead D T, 1992, *Phys. Med. Biol*. **37,** 1841.

[135] Uehara S, Nikjoo H, Goodhead DT, 1993, Cross-sections for water vapor for the Monte-Carlo electron track structure code from 10eV to the MeV region, *Phys. Med. Biol*. **38,** 1841-1858.

[136] Uehara S, Nikjoo H, Goodhead D T, 1999, Comparison and assessment of electron cross sections for Monte-Carlo track structure codes *Radiat. Res*. **152,** 202-213.

[137] Uehara S, Toburen L H, Nikjoo H, 2001, Development of a Monte-Carlo track structure code for low-energy protons in water, *Int. J. Radiat. Biol*. **77**, 139-154.

[138] Vriens L, 1966, Binary-encounter electron-atom collision theory, *Phys. Rev*. **141,** 88-92.

[139] Vriens L, 1969, Case Studies in Atomic Collision Physics, vol **1**, ed E W McDaniel and M R C McDowell (*Amsterdam: North-Holland*), 335.

[140] Vroom D A, Palmer R L, 1977, *J. Chem. Phys*. **66,** 3720.

[141] Ward J F, 1994, The complexity of DNA damage–relevance to biological consequences, *Int. J. Radiat. Biol*. **66,** 427-432

[142] Watanabe N, Hayashi H, Udagawa Y, 2000, Inelastic X-ray scattering study on molecular liquids, *J. Phys. Chem*. **61**, 407-409.

[143] Wilson W E, Nikjoo H, 1999, A Monte-Carlo code for positive ion track simulation, *Radiat. Environ. Biophys*. **38,** 97-104.

[144] Wilson W E, Paretzke H G, 1981, *Radiat. Res.* **81,** 521.

[145] Wilson W E, Miller J H, Toburen L H, Manson S T, 1984, *J. Chem. Phys*. **80,** 5631.

[146] Wilson W E, Metting, N F, Paretzke H G, 1988, Microdosimetric aspects of 0.3- to 20-MeV proton tracks. *Radiat. Res*. **115**, 389-402.

[147] Wilson W E, Paretzke H G, 1981, Calculation of distributions for energy imparted and ionization by fast protons in nanometer sites. *Radiat. Res*. **87**, 521-537.

[148] Wingate C L, Baum J W, 1976, Measured radial distributions of dose and LET for alpha and protons in Hydrogen and tissue-equivalent gas, *Radiat. Res*. **65**, 1-19.

[149] Xapsos M A, 1992, *IEEE Trans. Nucl. Sci*. **39,** 1613.

[150] Xapsos M A, 2001, *Nucl. Instr. and Meth.* B **184,** 113.

[151] Xapsos M A, 1992, A spatially restricted linear energy transfer. *Radiat. Res*. **132**, 282-287.

[152] Zaider M, 1991, Charged Particle Transport in the Condensed Phase, *Physical and Chemical Mechanisms in Molecular Radiation Biology* (New York: Plenum), 137.

[153] Zaider M, Bardash M, Fung A, 1994, Molecular damage induced directly and indirectly by ionizing radiation in DNA *Int. J. Radiat. Biol*. **66,** 459-465.

[154] Zaider M, Brenner D J, Wilson W E, 1983, The application of track calculations to Radiobiology: I. Monte-Carlo simulation of proton tracks, *Radiat. Res.* **95,** 231-247.

[155] Zaider M, Dicello J F, Horowitz Y, 1999, *Radiat. Prot. Dosim*. **82,** 163.

[156] Zaider M, Fry J L, Orr D E, 1990, *Radiat. Prot. Dosim*. **31,** 23.

[157] Zaider M, Vracko M G, Fung A Y C, Fry J L, 1994, *Radiat. Prot. Dosim*. **52,** 139.